THESIS FOR THE DEGREE OF DOCTOR OF PHILOSOPHY IN SOLID AND STRUCTURAL MECHANICS

Experimental Validation and Applications of a Phased Array Ultrasonic Testing Probe Model

XIANGYU LEI

Department of Industrial and Materials Science (IMS)
Division of Engineering Materials
CHALMERS UNIVERSITY OF TECHNOLOGY

Göteborg, Sweden 2023

Experimental Validation and Applications of a Phased Array Ultrasonic Testing Probe Model
XIANGYU LEI
ISBN 978-91-7905-718-3

© XIANGYU LEI, 2023

Doktorsavhandlingar vid Chalmers tekniska högskola
Ny series nr 5184
ISSN 0346-718X
Department of Industrial and Materials Science (IMS)
Division of Engineering Materials
Chalmers University of Technology
SE-412 96 Göteborg
Sweden
Telephone: +46 (0)31-772 1000

Cover:
Beam forming in steering and focusing case using a 16-element linear phased array probe with non-linear delay law

Chalmers Reproservice
Göteborg, Sweden 2023

Experimental Validation and Applications of a Phased Array Ultrasonic Testing Probe Model

XIANGYU LEI
Department of Industrial and Materials Science (IMS)
Division of Engineering Materials
Chalmers University of Technology

Abstract

New manufacturing technologies are developed to facilitate flexible product designs and production processes. However, the quality of the final products should not be compromised. The assessment of product quality and integrity lies on various inspection methods. Ultrasonic testing, among other nondestructive testing methods, is widely used as an effective and cost-efficient approach. The phased array technique in the field of ultrasonic testing shows more advantages over conventional technique and is revealing more benefits to industrial applications. To incorporate new technique into practice, it needs to be qualified with experiments. Due to the extensive costs and considerable challenges in experiments, the necessity of researching on reliable numerical models arises and several models had therefore been developed. The mathematical model implemented in the software, *simSUNDT*, developed at the Scientific Center of NDT (SCeNDT) at Chalmers University of Technology is one of these models for ultrasonic inspection. However, the validity of the models should be proved before supporting or replacing some of the experiments, which should ultimately be accomplished by experiments.

In this thesis, the main purpose is thus to further validate the phased array probe model in *simSUNDT* by comparing simulation with corresponding experiments. An experimental platform is built to fully control the operation conditions and the set of testing results. Well-defined and representative artificial defects in test specimens are manufactured and inspected under some inspection cases in both simulations and experiments. Comparisons in the end show good correlations.

Upon validation of the probe model, it is used in several application attempts for possible technique developments. This includes optimization of the generated sound field from a phased array probe and verifying the validity of the used log-normal probability of detection model. The basic ability of generating full matrix capture inspection dataset is also explored. This could provide a simulation scheme for parametric studies to investigate an ultrasonic imaging algorithm, total focusing method, in terms of its defect characterization capabilities.

Keywords: Nondestructive testing (NDT), Phased array ultrasonic testing (PAUT), Experiments, Simulations, Applications

Preface

The thesis includes the research work conducted during the year 2018 - 2022 under the framework of a joint research project *Adaptive Nondestructive Testing of Additive Manufacturing* (*Adaptiv oförstörande provning vid additiv tillverkning* på Svenska). This project is a collaboration between GKN Aerospace Engine Systems and Chalmers University of Technology, funded by the Swedish innovation agency VINNOVA (reference number 2017-04856) within the national aeronautical research program (NFFP7). The actual work was carried out at the research group of Advanced Nondestructive Testing, department of Industrial and Materials Science, Chalmers.

It is fruitful for me to study at Chalmers and I am very grateful to my supervisor Prof. Håkan Wirdelius. He enlightened me that research work is all about finding and exploring possible routes in dark, and there is no unique answer along the way. Whenever I drowned myself in dead ends, he always pulled me out by his ideas. I also appreciate the generous assistance from my co-supervisor Anders Rosell from GKN and Johan Carlson from Luleå University of Technology in all forms of discussions and guidance, and my examiner Thomas Abrahamsson at Chalmers for helping me out in my study life. The technical assistance of Farham Farhangi, Daniel Snögren and Jorge Benítez from the Swedish Qualification Centre (SQC) and Mattias Broddegård from Siemens Energy are also highly appreciated when I took my fingerprint on experimental works. Furthermore, I also want to say thanks to other members in our research group!

Finally, I am really grateful to my beloved family that always support and encourage me in China, and to my best friend Hao Wang staying with me when I was in hard time.

Gothenburg, 2023
Xiangyu Lei

Thesis

This thesis consists of an extended summary and the following appended papers:

Paper A Xiangyu Lei, Håkan Wirdelius, Anders Rosell. "Experimental validation of a phased array probe model in ultrasonic inspection". *Ultrasonics* **108** (2020): 106217.

Paper B Xiangyu Lei, Håkan Wirdelius, Anders Rosell. "Experimental Validation and Application of a Phased Array Ultrasonic Testing Model on Sound Field Optimization". *Journal of Modern Physics* **12**.4 (2021): 391-407.

Paper C Xiangyu Lei, Håkan Wirdelius, Anders Rosell. "Simulation-based Investigation of a Probability of Detection (POD) Model using Phased Array Ultrasonic Testing (PAUT) Technique". *Journal of Nondestructive Evaluation* **41**, 40 (2022).

Paper D Xiangyu Lei, Håkan Wirdelius, Johan Carlson. "The effect of ultrasound wave path estimation to defect characterization capability in half-skip total focusing method". *Submitted to conference.*

Paper E Xiangyu Lei, Håkan Wirdelius, Johan Carlson. "Model-based parametric study of surface-breaking defect characterization using half-skip total focusing method". *Submitted to journal.*

Other publications related to thesis:

Publication I Claudia Schwerz, Ahmad Raza, Xiangyu Lei, Lars Nyborg, Eduard Hryha, Håkan Wirdelius. "In-situ detection of redeposited spatter and its influence on the formation of internal flaws in laser powder bed fusion". *Additive Manufacturing* **47** (2021): 102370.

The appended papers were collaboratively prepared with co-authors. The author of this thesis was responsible for the major progress of the work, i.e. designing and performing of experiments, simulations, post-processing and writing of the papers, all with the assistance of the co-authors.

Contents

Abstract i

Preface iii

Thesis v

Contents vii

I Extended Summary 1

1 Introduction 1
1.1 Project background . . . 1
1.2 Research aims and limitations . . . 3
1.3 Thesis structure . . . 3

2 Technical Background 4
2.1 Ultrasonic Testing (UT) . . . 4
2.2 Phased Array Ultrasonic Testing (PAUT) . . . 5
2.3 Full Matrix Capture (FMC) and Total Focusing Method (TFM) . 9
2.4 simSUNDT . . . 10

3 Experimental validation of PA probe model 13
3.1 UT equipment . . . 14
3.2 Mechanized gantry system . . . 15
3.3 Test specimens . . . 15
3.4 Design of validation experiments . . . 17
3.5 Overview of validation results . . . 19

4 Applications of the PA probe model 20
4.1 Sound field optimization . . . 20
4.1.1 Nelder-Mead Simplex optimization algorithm . . . 20
4.1.2 Simulation scheme . . . 20
4.1.3 Results . . . 21
4.2 Simulation-based POD investigations . . . 22
4.2.1 Background of POD . . . 22
4.2.2 Expression of POD . . . 23
4.2.3 Modelling of POD function . . . 24

4.2.4 Motivation of simulation-based POD study 25
4.2.5 Simulated inspection scenario and handling 26
4.2.6 Results 27
4.3 Investigation of TFM by simulated FMC dataset 29
4.3.1 Generating FMC dataset by simSUNDT implementation . . 29
4.3.2 Snell's law based wave mode conversion in half-skip TFM . 31
4.3.3 Parametric studies of defect characterization using HSTFM 31
4.3.4 Results 33

5 Summary of appended papers **35**
5.1 Paper A 35
5.2 Paper B 35
5.3 Paper C 35
5.4 Paper D 36
5.5 Paper E 37

6 Concluding remarks **38**

References **40**

II Appended Papers A–E **45**

III Other Publications **119**

Part I
Extended Summary

1 Introduction

Ultrasound as a medium of Nondestructive Evaluation (NDE) and Nondestructive Testing (NDT) has been used for centuries in both medical and industrial fields thanks to its rapid and safe characters.

As indicated by its nomination, the ultrasonic wave is the sound wave that vibrates at frequencies over 20 kHz. Typical frequencies used in ultrasonic NDE applications are ranged from 50 kHz to some MHz. The essence of using ultrasound to perform evaluation and characterization is that the sound waves can propagate in materials. The features of propagation such as wave velocity and attenuation, can be used to characterize material properties in terms of its structure, elastic properties, etc. When propagating in an object, the waves interact differently to the variations. As an example in a fabricated structure, when encountering a pore (air) that has a different density to the surrounding materials, the waves scatter so that one can detect these scattered echoes and have an understanding of the different composition inside the object.

Today, many industries are using ultrasound as one of the inspection media to ensure the structural integrity and quality of the manufactured components. New techniques in this area are continuously developing along with the arising and application of the new manufacturing technologies.

1.1 Project background

In aerospace industries, advanced production and lightweight technologies are developed with the aim of fulfilling the increasing demands of aeroengines manufacturing with low environmental impact and reduced fuel consumption. This includes for example, Additive Manufacturing (AM), which enables effective manufacturing, materials utilization and energy optimization. However, new manufacturing technologies come along with problems, e.g. heat caused deformation and the appearance of unknown vital defects inside the components, which specifically relate to the production process. Thus, the application of these new production technologies demands higher and more reliable inspection methods for quality insurance and to maintain certain safety margins. Destructive testing (cut-up) is one way of inspection, but it is costly, unsustainable and the destroyed components could not be used any longer, which is not suitable for small quantity of production.

To overcome these drawbacks and to enable quality assessment at an early stage, NDT methods are to be considered.

Ultrasonic Testing (UT), among other NDT methods, has been proven to be an effective and powerful inspection method in this context. Phased Array Ultrasonic Testing (PAUT), is even more advanced that enables flexible and faster operations using a Phased Array (PA) ultrasonic probe, comparing to the conventional UT using single-element probe.

To confidently and formally apply the inspection techniques and corresponding evaluation procedures to the new manufacturing technologies, comprehensive qualifications must be performed on both inspection technique and related personnel [1]. Traditionally, this qualification is based on extensive practical experiments on various test specimens. This indicates that many variables should be characterized and limited to situations related to the specific application scenario. In addition to the massive cost of producing representative test specimens, the challenges of introducing characterized defects in critical locations are also considerable. However, such experiments could be assisted or even partly be replaced by mathematical models of the inspection methods, which had been developed in recent decades [2, 3]. These models include such as CIVA [4, 5], Thompson-Gray Measurement Model used in UTSim [6], Finite Element Method (FEM) model [7, 8], Elastodynamic Finite Integration Technique (EFIT) [9, 10], etc. With the help of these models, the corresponding experiments can be emulated numerically and the involved physical principles can be studied for further development. For instance, Azar et al. [11] took advantage of a numerical model to simulate the sound pressure field of a PA probe in beam steering and focusing cases, to show e.g. the impact of focusing towards the resolution of detection in the near field. Puel et al. [12] utilized numerical simulation with an evolutionary algorithm based optimization method to reach an optimal design and setting of PA probe.

It should be noted that the mathematical models should be thoroughly validated before application. This is performed either by comparing the model with other validated models, or by comparing the model with experimental results. Notice that experimental validations should ultimately be done in order to show that the model truly reflects the reality [13, 14].

An UT mathematical model, *UTDefect*, is implemented into a software, *simSUNDT*, developed by Chalmers University of Technology [15]. The conventional UT probe model involved has been validated [16–18] by comparing the simulation with the experimental benchmark studies [19], which was started by the World Federation of NDE Centres and the experimental results were provided by Commissariat a l'énergie atomique (CEA, France). The PA probe model [20] however, was validated only to a limit extent and thus requires further validations.

1.2 Research aims and limitations

This thesis is part of a joint research project *Adaptive Nondestructive Testing of Additive Manufacturing*. The overall objective is to incorporate the developed tools into inspection technologies during manufacturing processes, with the intention of quality control and assessment. The tool should also be optimized towards well-defined manufacturing defects, which potentially may occur in manufacturing processes. To accomplish this goal, the ultrasonic wave propagation within complex geometries should be studied through corresponding mathematical models. The overall research questions are e.g., how well the mathematical models can reflect on the physical inspections; what flexibility can be provided by the models; how can the models help with production and process optimizations, etc.

The thesis work thus aims mainly at further experimental validation of the newly developed PA probe model in the software, *simSUNDT*. Upon validation of the PA probe model, it is then explored in various application possibilities. This include:

- Sound field optimizations towards a backwall surface-breaking defect, with the intention of retrieving a maximized corner echo.
- Simulation-based investigation of Probability of Detection (POD), with the intention of exploring and investigating the validity of applied log-normal POD model.
- Generating simulated Full Matrix Capture (FMC) dataset, which enables some investigations and parametric studies of the algorithm of Total Focusing Method (TFM) for ultrasonic imaging.

However, some limitations are involved in the validation work. The considered defects only address some well-defined artificial types, i.e. side-drilled hole and surface-breaking defect. Source of attenuation including material damping properties of the test specimen and contact conditions that could influence beam divergence characters are not included in the corresponding simulations. This is justified that the validation focus is on the PA probe model instead of on material properties. These limitations could to some extent provide error source to the validation results.

1.3 Thesis structure

This thesis is structured in following sections according to the aims. Section 1 provides background information as well as the objectives and limitations of the

current work. Section 2 introduces basic knowledge related to the ultrasonic testing method and this thesis. The software *simSUNDT* is also briefly introduced with theoretical base and capabilities. Section 3 summarizes experimental validation works of the probe model. After the validation, it is in Section 4 that different application attempts are reviewed, including sound field optimizations, simulation-based POD investigations and parametric studies of FMC-TFM. Section 5 lists the summary of appended papers of the thesis. The extended summary ends with Section 6, where some concluding remarks are provided.

2 Technical Background

2.1 Ultrasonic Testing (UT)

The ultrasonic testing method is based on the ultrasonic waves generated from a specific transducer or probe. The essential part is the piezoelectric crystal that converts the imposed electrical pulse into mechanical movement (vibration), and vice versa. The generated acoustic waves can propagate in the inspected medium and scatter if striking on an object, e.g. pore or inclusion. Some of the scattered waves return back to the probe and are converted to electrical pulse by piezoelectric crystal. This output signal is represented as pulse amplitude versus elapsed time (Time-of-Flight, TOF), i.e. A-scan format in UT inspection. The line distance between the probe and the object can thus be determined given the wave traveling speed in the medium. Therefore, the ultrasonic testing method, like all other NDT methods, is indirect by nature, i.e. the measured outputs are in the form of A-scan and that other quantitative information are not directly obvious, e.g. the size of the object, which need further interpretations. B-scan and C-scan as two other result presentation formats, reorganize the A-scan data to help visualize object distribution within the inspected medium.

In practical applications, since the piezoelectric element is not a point source but has an area, the generated waves from each point of the area can interfere with each other constructively and destructively that end up with wave intensity fluctuations in certain distance, called *near field*. In relation to this, the region beyond that is called *far field* with minor intensity fluctuations. To avoid risk of measurement uncertainties from wave intensity fluctuations, most experiments are performed in the far field. The near field length N for a certain probe can be expressed by Equation (2.1), where λ is the wavelength and D is the diameter of a circular probe.

$$N = \frac{D^2}{4\lambda} \tag{2.1}$$

In most cases of UT, *longitudinal waves* and *transverse waves* are used in bulk materials. They are characterized by the movement directions of the medium particles. Different wave types can be converted, which is called *mode conversion* that happens when the waves strike on the material interface at an oblique angle. The waves can either be reflected or transmitted at the material interface with certain angles following *Snell's law*. It can be expressed in Equation (2.2) referring to Figure 2.1. Knowing the fact that the longitudinal waves generally travels faster than the transverse waves in mediums, the longitudinal wave angle should be larger than the transverse wave angle.

$$\frac{\sin\theta_i}{v_i} = \frac{\sin\theta_{rs}}{v_{rs}} = \frac{\sin\theta_{rl}}{v_{rl}} = \frac{\sin\theta_{ts}}{v_{ts}} = \frac{\sin\theta_{tl}}{v_{tl}} \tag{2.2}$$

where
θ_i - incident wave angle
θ_{rs} - reflected transverse wave angle
θ_{rl} - reflected longitudinal wave angle
θ_{ts} - transmitted transverse wave angle
θ_{tl} - transmitted longitudinal wave angle
v is the wave speed in corresponding medium for each case

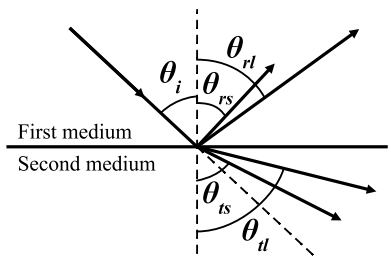

Figure 2.1: *Wave mode conversion and Snell's law demonstration*

2.2 Phased Array Ultrasonic Testing (PAUT)

The PA configuration generally refers to a series of transducers in an array setup, ordered linearly or in matrix form. PAUT therefore refers to an ultrasonic testing method that utilizes the specific probes, which consist of an array of small piezoelectric elements. The element shape is in most cases rectangular since

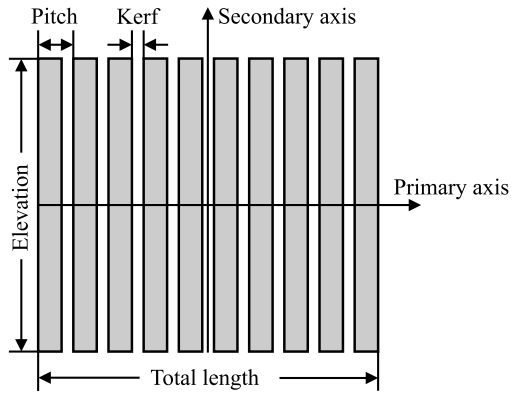

Figure 2.2: *The arrangement and terminology of a linear phased array probe*

they are cost-effective to produce. As an example, Figure 2.2 shows the linear arrangement of piezoelectric elements of a linear PA probe with corresponding terminologies. There are also other types of PA probes with overall angular shapes [21] in PAUT, but the linear and 2D (matrix) arrays are generally used in NDE.

Each of these small elements can be triggered individually by electronic pulse, and the signal response can also be recorded independently. In this way, sound beam *steering* and *focusing* can be easily accomplished through constructive interference of waves from each element comparing to conventional single-element UT. It also enables the possibility of fast visualization generation [21]. The key to this flexibility of PA probe is that each element can be driven individually with certain time shifts between pulses, called *delay law*. The synthetic wave front after constructive interference of each wave can therefore be a plane or focused wave propagating in certain direction depending on the applied delay law. It is also noted that the generated sound beam in the far field is similar to the one generated by the conventional single-element probe that has the same overall size as the PA probe. A general derivation of delay law for linear PA probe is presented in [22]. When each PA probe element receives signals, the corresponding delay law generally are used to process and sum up the individual signal to obtain a single output signal.

The advantage of using a PA probe is that the beam steering and focusing effect are obtained simply by adjusting the proper time delay laws, with no need of moving or changing the physical probe as in the conventional inspections. This flexibility enables many ultrasonic measurements in a rapid and simple way, for example a rapid sectorial scan in a region using a single PA probe and real-time imaging based on acquired data. Figure 2.3 shows an inspection case as an example, using a longitudinal wave linear PA probe on an AM specimen

(Titanium Alloy 6AL4V) with Side-drilled Holes (SDH) at depth of 14 mm. The SDHs under inspection have diameters of 1.2 mm, 0.8 mm and 0.4 mm from left to right. The probe contacts directly on the specimen surface and its position is unchanged as shown in the figure. The applied delay laws and the pulse sequences are: (a) 16-element aperture travels linearly along the array without focusing effect; (b) 16-element aperture travels linearly along the array with focusing at 14 mm depth; (c) 64-element aperture sectorial sweeping from -45° to 45° with focusing at 14 mm depth and (d) FMC that will be introduced in Section 2.3. The corresponding data visualization in B-scan can be seen in Figure 2.4, where the FMC data is visualized using an advanced imaging algorithm, TFM, also introduced in Section 2.3. It can be noticed in Figure 2.4(a)-2.4(c) that weaker ghost indications are also visible below the SDH indications, which could come from bottom sphere reflections and wave mode conversion, whereas the ghost indications are eliminated in Figure 2.4(d) by TFM.

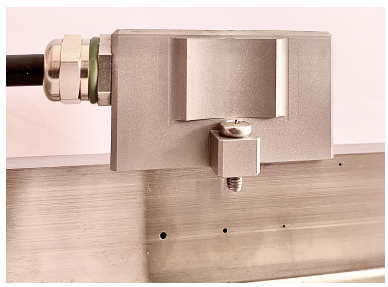

Figure 2.3: *PA probe inspects an AM specimen with SDHs (diameter of 1.2 mm, 0.8 mm and 0.4 mm from left to right) at depth of 14 mm from scanning surface*

This mentioned flexibility and feasibility of PAUT is further applied in a practical work aiming at detecting and verifying the existence of internal defects in laser powder bed fusion (**Other publication I**). A 64-element longitudinal wave linear PA probe was used in the study. To visualize the internal structures in a fast and easy way when the PA probe locates at a fixed position, 0° linear scan pattern (16-element aperture with step of 1 element) with focusing effect was applied on the built specimens. As comparison, FMC-TFM was also used on all specimens. The B-scan pictures for one of the test specimens having most internal defects are shown in Figure 2.5 as an example.

The near field length of a general rectangular PA probe can also be calculated using Equation (2.1), where the probe diameter D is now the total length of the PA probe (see Figure 2.2) if the aspect ratios between the total length and the elevation is larger than 0.6 [23]. By focusing effect, the resolution within PA probe's near field can be improved [11], as compared by Figure 2.4(a) and Figure

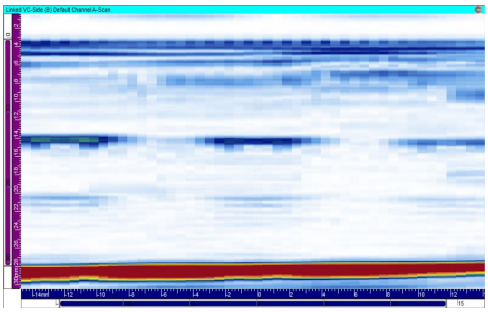

(a) Linear scan without focus

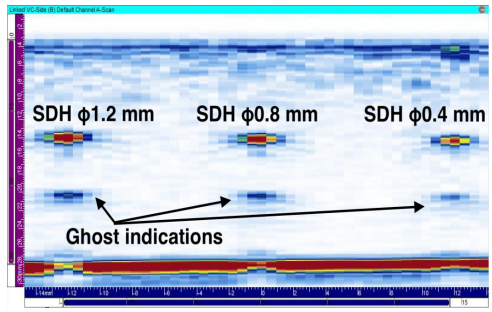

(b) Linear scan with focus at SDHs

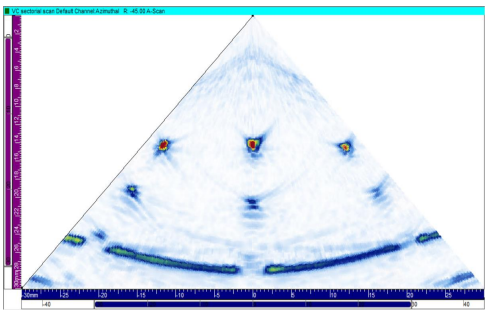

(c) Sectorial scan

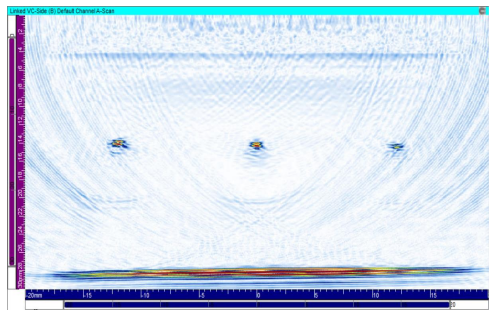

(d) TFM algorithm

Figure 2.4: *Four B-scans of flexible scanning and imaging possibilities using PA probe on an AM specimen with SDHs in the middle, as the case shown in Figure 2.3*

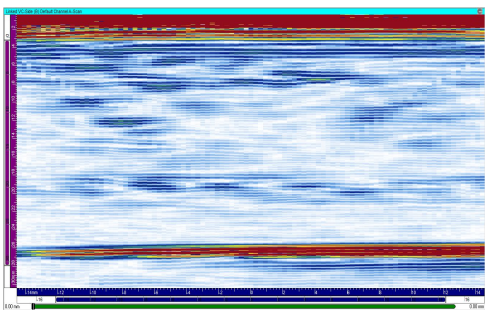

(a) Linear scan with beam focusing

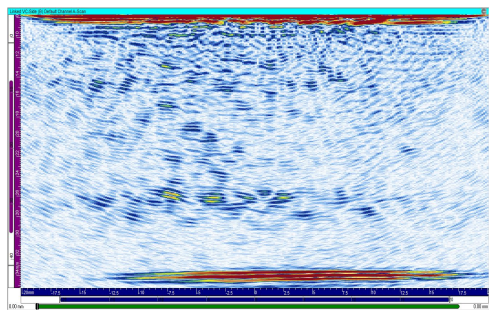

(b) FMC-TFM

Figure 2.5: *B-scans of a test specimen in laser powder bed fusion by linear scan sequence and FMC-TFM using a 64-element linear PA probe*

2.4(b).

Because of these advantages, PAUT had been applied in medical applications since decades [24, 25] and is now attracting more attentions from the industrial perspectives. For example, Shan et al. [26] built up an PAUT inspection system for defect detection in steel structures. A SDH in the test block can be quantitatively evaluated from the system. Lopez et al. [27] explored the possibility of using PAUT on AM specimen inspections and it was concluded to be suitable also for quantitative evaluations. Qin et al. [28] introduced an improved delay law calculation for PAUT technique based on the relation between the observed peak offset and propagation distance in high-density polyethylene used in the nuclear power plant pipes, in order to improve the ultrasound field intensity at the focal point of interest and to increase the imaging sensitivity. Gros et al. [29] discussed about more applications and the advantages of using PAUT in industries, as well as the necessity of numerical modeling and some future development possibilities of the technique.

2.3 Full Matrix Capture (FMC) and Total Focusing Method (TFM)

FMC is a data acquisition strategy using an ultrasonic PA probe to capture complete set of time-domain signals (A-scan) from every possible pair of transmitter-receiver combination, e.g. A-scan signal from i-th element (transmitter) to j-th element (receiver), S_{ij}, illustrated in Figure 2.6. In this way an array with N elements can generate N^2 possible A-scan data by FMC, i.e., S_{ij} with i, j=1, ..., N. This complete set of A-scan data can provide any beam-forming scheme of conventional PAUT in the post-processing with no need of extra experiments [30].

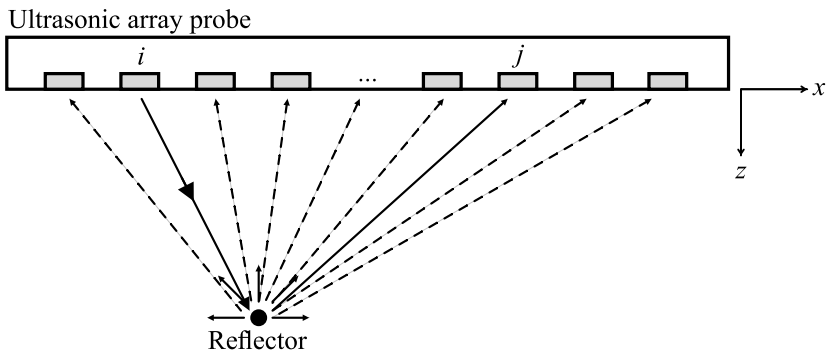

Figure 2.6: *FMC illustration with the i-th element as transmitter*

To take the full information from FMC dataset, an imaging algorithm, TFM [31], is preferred, which has better imaging performance comparing to conventional algorithms [30], see also comparisons in Figure 2.4. The imaging process is performed by firstly discretizing the imaging region of interest into discrete grid of imaging pixels, then taking the signal amplitude from all transmitter-receiver pairs in FMC A-scans at the corresponding TOF of each element pair to the imaging pixel, P. The image is finally formed by summing all these signal amplitudes at this pixel and repeating for all image pixels, as expressed in Equation (2.3) referring to Figure 2.7(a) for the direct path reconstruction mode. Considering the complexity of wave propagation possibilities in a test specimen, half-skip and full-skip path reconstruction modes are proposed [32], which account for the situations that either one wave path (Figure 2.7(b) and Equation (2.4)) or both paths (Figure 2.7(c) and Equation (2.5)) rebound on specimen backwall, respectively. These different modes of TFM algorithm complement each other since the imaging quality of modes is strongly sensitive and dependent on certain defect characteristics [33, 34]. Due to massive computation effort, TFM imaging is practically performed during post-processing.

$$I_{TFM}(P) = \sum_{i=1}^{N} \sum_{j=1}^{N} S_{ij}(t = TOF_{iP} + TOF_{Pj}) \tag{2.3}$$

$$I_{TFM}(P) = \sum_{i=1}^{N} \sum_{j=1}^{N} S_{ij}(t = TOF_{iB} + TOF_{BP} + TOF_{Pj}) \tag{2.4}$$

$$I_{TFM}(P) = \sum_{i=1}^{N} \sum_{j=1}^{N} S_{ij}(t = TOF_{iB} + TOF_{BP} + TOF_{PR} + TOF_{Rj}) \tag{2.5}$$

2.4 simSUNDT

The *simSUNDT* software consists of a Windows®-based pre- and post-processor, as well as a mathematical kernel *UTDefect* [17, 35] that conducts the actual mathematical modeling and computation. *UTDefect* was developed at Chalmers University of Technology. The 3D elastodynamic wave equation, which defines the wave propagation in a homogeneous half space, is solved using vector wave functions [35].

The contact probe can be modeled in elliptic and rectangular shape. The modeling assumes that the probe is placed on the surface of an elastic half-space, which has no traction on the surface except beneath the probe. This enables

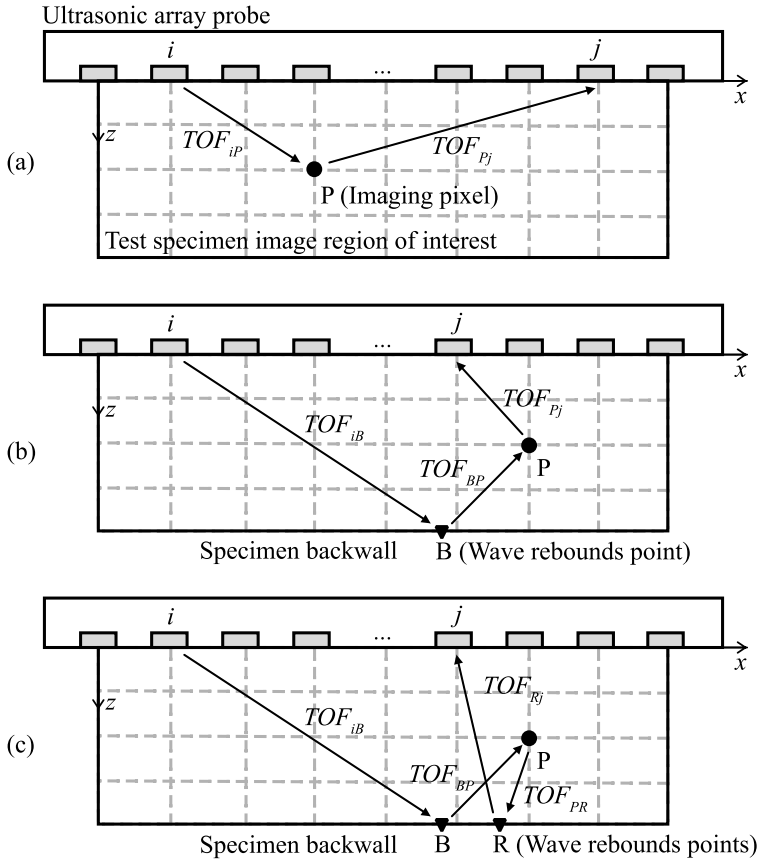

Figure 2.7: *Illustration of different wave paths used in TFM with (a) direct path, (b) half-skip path and (c) full-skip path*

the possibilities of simulating any types of the probe available on the market, by specifying related parameters such as wave types, element size and shape, angles, frequency ranges, contact conditions, etc. The traction is derived so that a plane wave is generated in the far field, shown in Equation (2.6) for longitudinal, vertical transverse (SV) and horizontal transverse (SH) wave types, respectively.

$$\mathbf{t} = \begin{cases} Agi\mu k_p[(k_s^2/k_p^2 - 2\sin^2\gamma)\hat{z} + \delta \sin 2\gamma \hat{x}]e^{-ik_p x \sin\gamma}, \text{Longitudinal probe} \\ Agi\mu k_s[\sin 2\gamma \hat{z} - \delta \cos 2\gamma \hat{x}]e^{-ik_s x \sin\gamma}, \text{SV probe} \\ Agi\mu k_s \delta \cos\gamma \hat{y} e^{-ik_s x \sin\gamma}, \text{SH probe} \end{cases} \tag{2.6}$$

where $\hat{x}$, $\hat{y}$ and $\hat{z}$ are the unit vectors in corresponding directions. A is the

displacement amplitude and the function g enables reduction of edge effects. μ is the Lamé constant of the elastic half space. k_p and k_s are longitudinal and transverse wave numbers, respectively. γ is the wave angle. $\delta \in [0,1]$ is a constant that represents the coupling effect, where δ=0 is fluid coupling and δ=1 is glued condition.

The wave propagation is governed by the elastodynamic equation of motion, in which the displacement field, $\mathbf{u}$, is given by:

$$k_p^{-2}\nabla\nabla\cdot\mathbf{u} - k_s^{-2}\nabla\times\nabla\times\mathbf{u} + \mathbf{u} = \mathbf{0} \tag{2.7}$$

The total displacement field is a summation of the incident field ($\mathbf{u}^i$) and the scattered field ($\mathbf{u}^s$), as:

$$\mathbf{u} = \mathbf{u}^i + \mathbf{u}^s \tag{2.8}$$

The incident fields can be expanded in terms of regular spherical partial vector waves ($\mathrm{Re}\boldsymbol{\Psi}_n$), and the scattered field caused by various of defects can be expanded in its outgoing spherical partial vector waves ($\boldsymbol{\Psi}_n$):

$$\begin{cases} \mathbf{u}^i = \sum_n a_n \,\mathrm{Re}\,\boldsymbol{\Psi}_n \\ \mathbf{u}^s = \sum_n f_n \boldsymbol{\Psi}_n \end{cases} \tag{2.9}$$

Volumetric and crack-like defects are available types of defect to be modeled. Specifically, volumetric defects include a spherical/spheroid cavity (pore), a spherical inclusion (isotropic material differing from the surrounding material, i.e. slag) and a cylindrical cavity (SDH). Crack-like defects include rectangular/circular crack (lack of fusion) and strip-like crack (fatigue crack). There is option to model the surface roughness for the rectangular and strip-like crack, and the degree of closure can be modeled for the circular crack. Tilting planar back surface could also be modeled for the strip-like crack, but otherwise it is assumed parallel to the scanning surface. The surface-breaking strip-like crack and rectangular crack close to the back surface can be used to model the corresponding defects in the test piece.

The modeling of these defects are important and the methods of solution can be for example, various types of surface integral equations, null field approach (T-matrix method) and FEM. *UTDefect* incorporates the T-matrix method [36] and all information regarding the defects is included in the transition matrix, as well as providing the linear relation between the expansion coefficients of the incoming (a_n) and scattered (f_n) wave fields in Equation (2.10):

$$f_n = \sum_{n'} T_{nn'} a_{n'} \tag{2.10}$$

To incorporate the probe model into the T-matrix formulation, the displacement field needs to be transformed from the plane vector waves centered at the contact area into spherical vector wave functions oriented and centered at the defect [35].

To model the receiver, a reciprocity argument [37] is applied. In the end, the electrical signal response is expressed in Equation (2.11) with the transmitting probe characterized by $a^a_{n'}$, the defect by $T_{nn'}$ and the receiving probe by a^b_n.

$$\delta\Gamma \sim \sum_{nn'} a^b_n T_{nn'} a^a_{n'} \tag{2.11}$$

To simulate the entire testing procedure of an actual NDT situation, a calibration option is available towards a reference reflector including for example, the SDH represented by the cylindrical cavity [38] and the *flat-bottomed hole* (FBH) approximated by an open circular crack.

The model geometry can be limited by a reflecting backwall and be described as a plate with finite or infinite thickness bounded by the scanning surface, on which the scanning sequence are defined by rectangular mesh.

In addition, it is also possible to suppress the unexpected wave component in the simulation to eventually facilitate the analysis of the received signal. The configurations of the probe can be chosen among pulse-echo, separate with fixed transmitter and tandem configuration (TOFD).

These principles are the same for the phased array probe model, that element is represented by the boundary conditions (traction), from which the plane wave is generated in the far field with a certain angle. The individual boundary conditions are translated into the main coordinate system and a phased array wave front with certain nominal angle is formulated by constructive phase interference. The formulated nominal angle can also be altered by specific delay law, but it should be noted that this is only possible for small angles if no wedge is specified.

3 Experimental validation of PA probe model

This section summarizes the experimental setup for validation works of the PA probe model, including the UT equipment, the mechanized gantry system, the test specimens used in the experiments, and the design of experiments (DOEs). The section ends up with an overview of some results.

3.1 UT equipment

The UT equipment mainly includes the data acquisition hardware (*TOPAZ64*®) from Zetec company and a commercial linear PA probe with corresponding plastic wedges from Zetec.

TOPAZ64® (Figure 3.1 (left)) is a portable 64-channel phased array ultrasonic testing equipment with FMC and TFM capabilities incorporated. Ultrasonic inspection data is communicated in real time between *TOPAZ64*® and computer by gigabyte ethernet cable connection, and is processed by corresponding software *UltraVision*® on the computer.

The commercial PA probe is a 64-element linear phased array longitudinal-wave probe with the notation of LM-5MHz (Figure 3.1 (right)). The nominal center frequency is 5 MHz and bandwidth is 74%. Refer to Figure 2.2, each element has a size of 0.5 mm along primary axis and 10 mm in secondary axis (elevation). The kerf between elements is 0.1 mm and the total aperture of the probe is thus 38.3 mm in primary axis and 10 mm in elevation.

Figure 3.1: *Data acquisition hardware unit, TOPAZ64*® *(left), and linear PA probe, LM-5MHz (right)*

Two probe-matched plastic wedges (Figure 3.2), with and without wedge angle denoted as LM-55SW and LM-0LW, respectively, are used in all experiments to protect the contact surface of the PA probe and to generate angled beam properly. The screw holes on two sides of the wedge facilitate fixation of the probe on mechanized system, and the screw holes on the wedge surfaces are used to fix the PA probe to ensure good surface contact. The angled wedge (LM-55SW, wave speed = 2330 m/s) helps the PA probe generate 55° transverse waves into carbon steel (wave speed = 3230 m/s) without any delay law according to Snell's law in Equation (2.2), or 40° to 70° transverse waves by certain delay laws.

Figure 3.2: *Plastic wedges, LM-55SW (left) and LM-0LW (right)*

3.2 Mechanized gantry system

The mechanized gantry system is built on the experimental platform (Figure 3.3 (left)) with the intention to provide a stable inspection and operation condition with high repeatability between experiments. Within the scope and purpose of the experiments, the gantry system is motor controlled only in the horizontal plane (x-y plane), while the z-axis position is manually adjusted by a guide screw on top. The movement patterns are electronically controlled by computer. The embedded encoders in the motors can provide position information in x-y plane, which enable different data presentation possibilities, e.g. B- and C-scan. During inspections, the water tank containing test specimens is placed on the platform and the wedge with PA probe is clamped on a beam in z-axis by a spring-loaded fork, as shown in Figure 3.3 (right). Water is used as couplant in all inspections. The level of water in tank is a bit higher than specimen top surface so that the bottom surface of plastic wedge is constantly submerged to transmit ultrasonic waves into test specimen.

3.3 Test specimens

Three flat surface test specimens (#1, #2, #3) with well-defined artificial defects are mainly used in the validation work, shown in Figure 3.4. The first one (#1, aluminum) has 15 SDHs (3 mm in diameter) at depth range from 20 mm to 90 mm in step of 5 mm, drilled through the width of specimen and one of the SDHs can be used as calibration defect. As mentioned in Section 2.4 that FBH could also be treated as the calibration defect in *simSUNDT* and in experiments, however, due to its manufacturing uncertainties [20], it is not considered in this work. The second test specimen (#2, stainless steel) has Electric Discharge Machined (EDM) notches on the specimen surface, denoted as surface-breaking cracks with height of

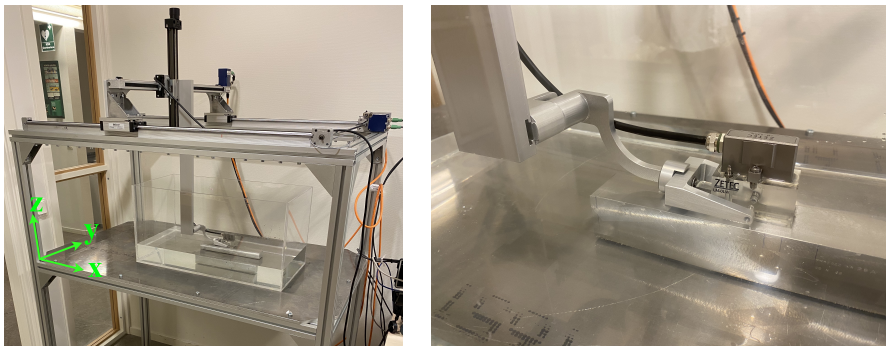

Figure 3.3: *Mechanized gantry system on the experimental platform (left) and probe fixation (right)*

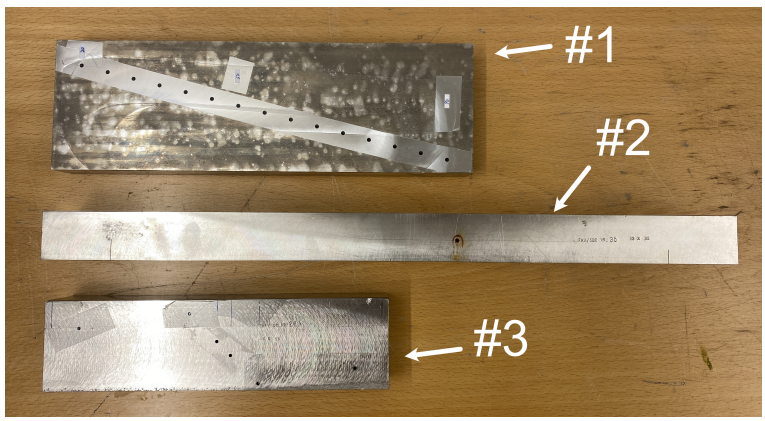

Figure 3.4: *Test specimens used in validation work*

15 mm, 0.5 mm, 2 mm, 5 mm and 10 mm, ordered as in the specimen. The third test specimen (#3, stainless steel) has 6 SDHs (2 mm in diameter) at depth range from 10 mm to 60 mm in step of 10 mm, drilled through the width of specimen.

The dimension and acoustic properties of these three test specimens are summarized in Table 3.1. The profile sketches of these specimens in length-height plane are shown in Figure 3.5.

$$\alpha_{dB/wavelength} = \frac{20\log_{10}(\frac{A_1}{A_2})}{\frac{2h}{\lambda}} = \frac{10\lambda\log_{10}(\frac{A_1}{A_2})}{h} \tag{3.1}$$

Table 3.1: Dimension and acoustic properties of three test specimens

No.	Length (mm)	Height (mm)	Width (mm)	L-wave speed (m/s)	T-wave speed (m/s)	Attenuation, α* (dB/wavelength)
#1	320	100	30	6320	3130	0.09
#2	500	35	50	5573	3150	0.11
#3	250	65	39	5640	3110	0.06

*The material attenuation property is characterized here in terms of attenuation coefficient α. It is calculated by Equation (3.1) based on Equation (3.94) in [39]. A_1 and A_2 are the amplitudes of the first two backwall reflections using the PA probe LM-5MHz (unfocused and 0° beam angle with only the center 16 elements activated), h is the specimen height and λ is the corresponding longitudinal wave length. These coefficients in this thesis only serve as an indication of relative low material attenuation property compared to Hastelloy X of $\alpha = 0.15$ dB/wavelength (material type used in **Other publication I**).

3.4 Design of validation experiments

By the availability of UT equipment, only one PA probe is used in all experiments, which limits the inspection configuration. Here, the pulse-echo mode is used in the experiments and simulations, where only one PA probe is acting as both transmitter and receiver. The validation of the probe model addresses the comparisons of the maximum echo amplitudes from SDHs on test specimen #1 (**Paper A**), data presentations in terms of A-, B- and C-scan towards defects on test specimen #2 and #3 (**Paper B**) between the experiments and corresponding simulations. Only the SDH at 50 mm depth in specimen #3 is used though.

In **Paper A**, the PA probe performs a continuous one-line scan on the scanning surface of test specimen #1 over all defects, as in the simulation. Inspection scenario includes non-angled and 45° angled sound beams with and without focusing effect. Only the central 16 elements are active in the unfocused inspection to avoid ghost images, whereas all 64 elements are active to generate proper focusing effect at certain depths of interest. The maximum echo amplitude of each defect, expressed in percentage of screen height in experiments, could be retrieved in post-processing. All inspection scenarios are experimentally repeated five times for averaging all values for a defect as a result, associated with mean value with variations. All maximum echo amplitudes of the defects (A_{def}) are normalized to the respective calibration SDH (A_{cal}) and expressed in decibel (dB) using Equation (3.2), where G_{def} and G_{cal} is the applied gain to the defect and calibration SDH amplitude, respectively. The results in dB are in comparison with corresponding simulations in the end.

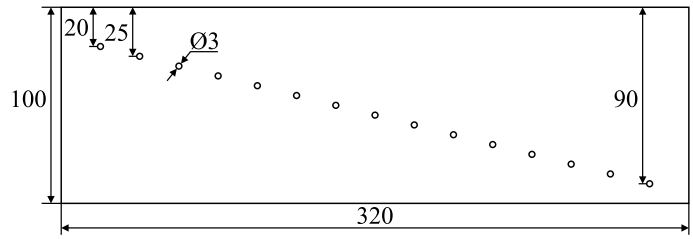

(a) Test specimen #1 with SDHs with depth from 20 mm to 90 mm in step of 5 mm

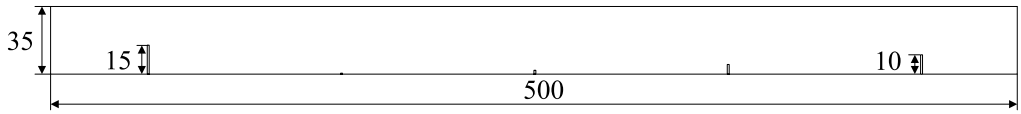

(b) Test specimen #2 with EDM notches with heights of 15 mm, 0.5 mm, 2 mm, 5 mm and 10 mm from left to right

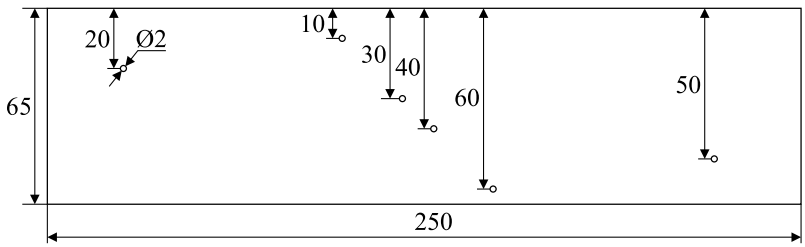

(c) Test specimen #3 with SDHs

Figure 3.5: *Sketch profiles of the test specimens*

$$dB = 20\log(\frac{A_{def}}{A_{cal}}) - (G_{def} - G_{cal}) \tag{3.2}$$

In **Paper B**, on test specimen #2, the PA probe performs a continuous one-line scan on the scanning surface with 45° angled sound beam. This is because the upright surface-breaking defects in specimen #2 give a corner echo from an angled incoming sound beam as the received signal. The inspection is performed with and without focusing effect at the specimen bottom. On test specimen #3, the PA probe scans only the SDH at 50 mm depth with non-angled and 45° angled sound beam with and without focusing effect at the center of this SDH. The direct echo is the received signal. Same as earlier, only the central 16 elements are active in the unfocused inspections and all 64 elements are active in focused inspections. In order to capture the maximum echo amplitude for detailed A-scan

and ensure a complete visualization of B-scan and C-scan (echo dynamic curve here under one-line scan configuration), all simulations are conducted in large scan and time intervals with refined scan increment and time step. This configuration is time-consuming to some defects with large size and complexity though.

3.5 Overview of validation results

The comparisons of maximum echo amplitude present good agreements between experiments and simulations in general, especially for inspection scenarios without focusing effect, where the mismatch is at most 2 dB for all involved defects. Potential reason for the mismatch could come from attenuation in terms of material damping (grain scattering and viscous damping), which is not included in the simulations. When respective focusing effect is considered, good agreement between experiments and simulations can be observed within the focusing depth range, i.e., focusing depth $\pm$ 5 mm. The potential reason for large discrepancy outside the focusing depth range could be the near field fluctuations of wave intensity far from the wave focus point providing that the probe aperture is large (38.3 mm) when all 64 elements are active, see Equation (2.1). It is also noticed through experiments that the difference between specified and actual focusing depth exists when the focusing point is beyond some depth, as Azar et al. indicated in beam simulations [11]. This difference would get even larger when the focusing point gets deeper, as found by Sun et al. [40]. Taking this phenomenon into consideration, some further simulations are performed with new focusing depth observed from experiments and improvement of result comparisons can be seen within the focusing depth range.

The comparisons of different data presentations in terms of A-, B- and C-scan also show overall good agreements and consistencies. The wave form in A-scan of the smallest crack with height of 0.5 mm on test specimen #2 does not correlate very well by simulation, probably because it stands more for a volumetric defect than an actual crack, which is actually modelled in simulation. Other reasons that might lead to minor difference in comparisons could be from variance of contact conditions and beam divergence.

Generally speaking, giving the comparisons presented from both perspectives, the implemented PA probe model can show satisfactory correlations to corresponding experiments, and can be confirmed to be a valid simulation model to assist further experimental work.

4 Applications of the PA probe model

By the experimental validation works, the validated PA probe model is then able to be applied in different investigations, for better understanding of this technique. The applications explored in this thesis include sound field optimizations by flexible parametric studies, investigation of simulation-based POD and parametric studies of TFM algorithm based on simulated FMC dataset.

4.1 Sound field optimization

The sound field optimization aims at searching for a proper combination of decision variables, i.e., delay law (combination of element delays) of PA probe so that an optimization objective (optimal or maximized echo amplitude from a defect with certain features) can be obtained (**Paper B**). This could form a basis to study the wave propagation and reflection from defects. The previous validated PA probe model is hereby used in parametric studies to investigate this optimization possibility and to search for the specific delay law.

4.1.1 Nelder-Mead Simplex optimization algorithm

For this non-linear single-objective (to maximize echo amplitude) optimization problem, an heuristic algorithm named Nelder-Mead Simplex method [41] is used. It starts by constructing vertices of a simplex, where each vertex contains a set of decision variable values. Then the objective values at simplex vertices are compared and evaluated to move the simplex towards the optimal solutions based on various strategies, i.e. reflection, expansion, contraction and shrink, see Figure 4.1 for simple illustration (vertex x_1 gives the best objective value and x_3 contains the worst in this case). The process iterates until certain optimization criteria is satisfied. It is noticed that this algorithm does not calculate the derivatives and is more robust than gradient-based algorithms, which motives the choice of this method.

4.1.2 Simulation scheme

Practically in this thesis work, the optimization algorithm and process is controlled using a workflow automation software, *modeFrontier*®. The mathematical kernel *UTDefect* is incorporated with *modeFrontier*® to generate, evolve, compute and evaluate signal responses according to Simplex method. For all optimization works, the simulated instruments are the same as in previous validation works (Section 3.1) for consistency and possible experimental verification. Within the

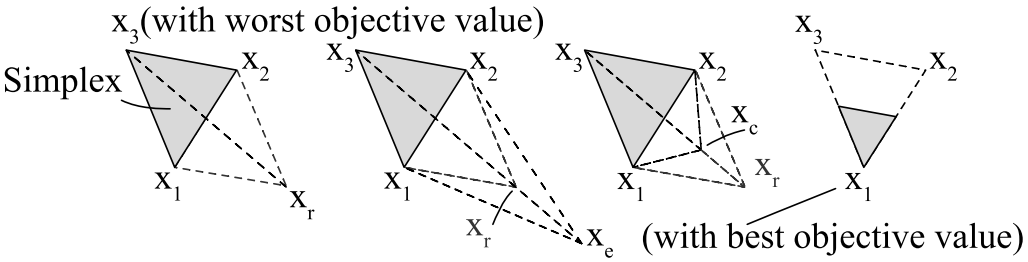

Figure 4.1: *Four operations in Nelder-Mead based Simplex optimization algorithm (left to right): reflection, expansion, contraction and shrink*

availability of control parameters of *UTDefect*, the equivalent decision variables in the current case are the beam angle and focus distance of the wave beam, which in the end provide a certain synthetic wave front as delay law does. The efficiency of iterating many simulations is also investigated with different probe frequency contents as full bandwidth of the PA probe LM-5MHz (74%), 0.02% bandwidth and monochromatic frequency (only the nominal center frequency without bandwidth). It is noticed from the study that simulations with 0.02% bandwidth can be time-saving and preserve the resulted echo amplitude as of full bandwidth, and monochromatic frequency can result in the same decision variables as of 0.02% bandwidth to the optimization problem, while saving massive simulation times and make it feasible to find optimal solution.

4.1.3 Results

The first sound field optimization work is conducted on a well-defined surface-breaking crack as in test specimen #2 in validation work (see Figure 3.5(b)). It is upright towards bottom surface and has a size of 10 mm located at the bottom surface. It is mostly presumed for this defect feature that a 45° beam angle with focusing depth at crack bottom (i.e. 35 mm in this case) will give a maximized corner echo amplitude, which results in 76.8 dB in *simSUNDT* simulation with full bandwidth. However, the iterative optimization process indicates that a 48° beam angle with focusing depth of 30.2 mm can give a larger corner echo amplitude of 80.2 dB using 0.02% bandwidth, shown in Figure 4.2 and echo amplitude of 80.9 dB using full bandwidth. This optimal solution of decision variables are also experimentally verified on test specimen #2.

By the above trial, another optimization attempt is then performed on a similar surface-breaking crack with 5° tilt angle. Figure 4.3 shows the iterative optimization process on this defect using monochromatic frequency. The optimal solution of decision variables are 56° beam angle with 26 mm focusing depth,

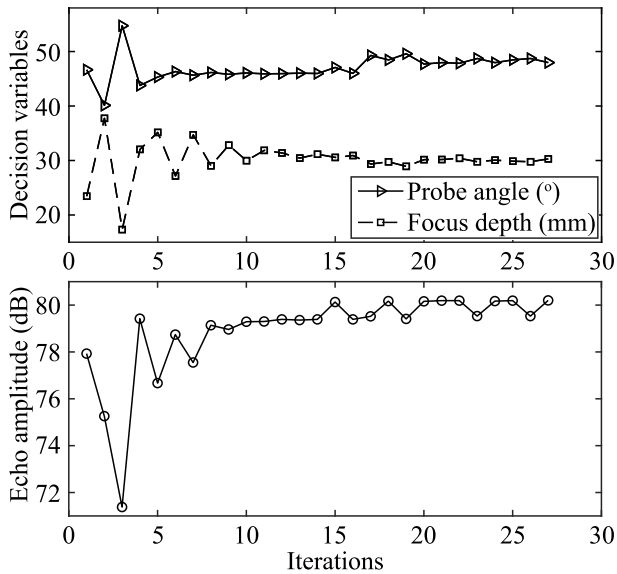

Figure 4.2: *Iterative sound field optimization process for the 10 mm height crack in test specimen #2 using a reduced probe frequency bandwidth of 0.02%*

which is also verified by using 0.02% bandwidth.

Briefly summarizing as mentioned earlier, 0.02% bandwidth preserves the resulted echo amplitude as of full bandwidth and monochromatic frequency can result in the same decision variables as of 0.02% bandwidth. It is hereby feasible to perform further optimizations based on monochromatic frequency because it is the decision variables (beam angle and focusing depth in this case) that matter in exploring the design space, and the optimization objective (resulted echo amplitude) can be finally obtained by using the optimal decision variables in corresponding simulation.

4.2 Simulation-based POD investigations

4.2.1 Background of POD

In manufacturing industries with safety-critical assets, it is essential to monitor and assess the production quality and to ensure the structural integrity of products. This puts high demands on the reliability of production processes and the corresponding inspection operations and procedures. For NDE process however, the inspection capability has intrinsic probabilistic characterization, which means that the repeated inspections of the same defect size or type will not necessarily

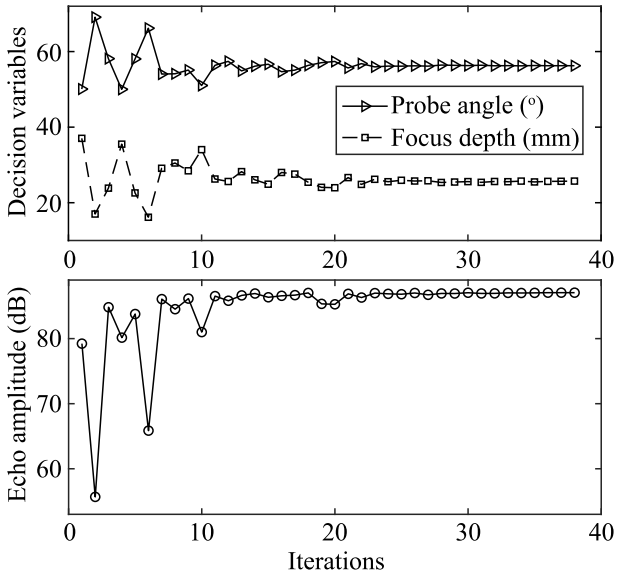

Figure 4.3: *Iterative sound field optimization process for the 10 mm height and 5° tilt angle crack using a monochromatic frequency*

give consistent results, e.g., hit or miss. In other words, there is a spread of detection results for each defect size and type. It is therefore of great importance to evaluate and quantify the performance of an NDE procedure.

The quantification of detection capability is expressed statistically in terms of POD [42], which is a statistic metric initiated since 1970s from aero industries [43]. The main purpose of POD is to describe the accuracy of an inspection procedure by revealing the capacity of detecting vital defects. Other aims of POD include e.g. establishing design acceptance requirements, NDE procedure and personnel qualification and acceptance, providing tools for comparing and selecting the alternative inspection techniques, etc. [42].

4.2.2 Expression of POD

The POD values are obtained by transforming a series of available inspection data into a relation between the probability of defect detection and a characteristic parameter of the defects (usually the defect size) [44]. The inspection data can be collected from e.g. field service records, artificially created defect blocks, etc. [45], where the inspections are repeated in many runs under a controlled condition specified by an inspection procedure. The obtained POD results are thus only valid under the applied inspection procedure. The recorded inspection data can

be classified into two types, one is *hit/miss* type if binary conclusions are drawn, another one is *signal response* type if result amplitudes are recorded. The POD value for a certain defect size "a" is then interpreted as the proportion of times the defect being detected among all attempts, formulated as Equation (4.1), where n_d is the number of times a defect of certain size is detected and n is the total number of detection attempts on this defect size. A POD curve (function) is then approximated with best fit through all POD values among a range of defect sizes.

$$POD(a) = \frac{n_d}{n} \tag{4.1}$$

Early on in the mid-1970's, a constant POD for all defect types of the same size was proposed and binomial distribution methods were used to estimate the probability [46, 47]. However, this assumption of constant POD for a given size was too simple and inaccurate since a study of the inspectors' capability shows variation in repeated measurements on a single defect and on different defects of the same size [48]. Practically, there are different factors that can introduce variations in determining the POD values, including NDE methods, equipment calibration, material conditions, defect characteristics and most importantly, human factors in manual inspection operations, as experienced inspectors usually have better detection probabilities. Thus, it is essential to understand how POD value is derived and to question its validity and limitations.

4.2.3 Modelling of POD function

In the early to the mid-1980's, the approach was to propose a more general statistical model for the POD curve as a function of defect size "a", i.e. $POD(a)$. Different methods and models for determining POD curve were presented and evaluated by Berens et al. [45] and it was indicated that the $POD(a)$ function could be modelled by *log-odds* (Equation (4.2)) and *cumulative log-normal* (Equation (4.3), also referred as Probit [45]) distributions for hit/miss type and signal response type of data (also written as "$\hat{a}$" vs. "a" data, where "$\hat{a}$" stands for signal response amplitude), respectively [49]. Symbol "Φ" in Equation (4.3) denotes standard normal distribution function, and the statistical parameters μ and σ can be estimated using standard statistical methods such as *maximum likelihood estimates*. It is also noted that these two distribution models are equivalent to each other provided that they share the same parameters.

$$POD(a) = \left(1 + exp - \left[\frac{\pi}{\sqrt{3}}\left(\frac{\ln(a) - \mu}{\sigma}\right)\right]\right)^{-1} \tag{4.2}$$

$$POD(a) = \Phi\left(\frac{\ln(a) - \mu}{\sigma}\right) = \Phi\left(-\frac{\mu}{\sigma} + \frac{1}{\sigma}\ln(a)\right) \tag{4.3}$$

Regarding the cumulative log-normal POD model for signal response type of data, it was originated from a basic approximation that there is a linear relation between the signal response ($\hat{a}$) and defect size (a) in such a way:

$$\ln(\hat{a}) = \beta_0 + \beta_1 \ln(a) + \delta \tag{4.4}$$

where β_0 and β_1 are the intercept and slope, and δ (assumed normally distributed with zero mean and constant standard deviation σ_δ that is independent on defect size [49]) stands for random error addressing the difference between observed and estimated signal response.

Based on this linear relation approximation in Equation (4.4), it can be seen in another way that $\ln(\hat{a})$ is assumed normally distributed with mean value of $\beta_0+\beta_1 \ln(a)$ and constant standard deviation of σ_δ, i.e., $\ln(a) \sim N(\beta_0+\beta_1 \ln(a), \sigma_\delta)$. Thus, the $POD(a)$ function can be calculated as:

$$\begin{aligned} POD(a) &= \text{Probability}[\ln(\hat{a}) > \ln(\hat{a}_{dec})] \\ &= 1 - \Phi\left[\frac{\ln(\hat{a}_{dec}) - (\beta_0 + \beta_1 \ln(a))}{\sigma_\delta}\right] \\ &= \{\text{Using symmetry property of } \Phi\} \\ &= \Phi\left[\frac{\ln(a) - \frac{ln(\hat{a}_{dec}) - \beta_0}{\beta_1}}{\frac{\sigma_\delta}{\beta_1}}\right] \end{aligned} \tag{4.5}$$

where $\hat{a}_{dec}$ is a chosen decision threshold for signal response, above which the defect is marked detected. Comparing Equation (4.5) with Equation (4.3), we can see that the two statistical parameters in Equation (4.3) are actually:

$$\begin{aligned} \mu &= \frac{ln(\hat{a}_{dec}) - \beta_0}{\beta_1} \\ \sigma &= \frac{\sigma_\delta}{\beta_1} \end{aligned} \tag{4.6}$$

4.2.4 Motivation of simulation-based POD study

Lots of studies regarding inspection capability and reliability under different inspection scenarios have been performed worldwide, and in recent decades most of the researches have been focused on investigating the feasibility of generating and complementing inspection data for POD estimations using physics-based NDT

simulation models [50–53]. *UTDefect* had also been utilized in this field on an inspection procedure UT-01 for pipes [54]. Comparing to physical experiments, the simulation models have the advantages of energy- and material-saving, feasibility of parametric studies on reliability and so on [55, 56]. However, the mentioned studies deployed the log-normal POD model directly on the simulated inspection data without careful consideration and evaluation of the involved assumptions, such as the linear relation and the random error term in Equation (4.4). In other words, there is a shortage of verification on the obtained $POD(a)$ function if the assumptions are not totally satisfied. This is therefore the motivation of current application work.

4.2.5 Simulated inspection scenario and handling

The validated PA probe model in *simSUNDT* is applied in this application work to generate a series of simulated inspection data (signal response data), which will be the basis for estimating the corresponding POD curve using log-normal POD model. The considered inspection scenario is PAUT on lack-of-fusion defect in some additive manufacturing processes (e.g., Laser Metal Deposition, LMD) using materials with acoustic properties similar to test specimen #2 in previous validation work (see Table 3.1), and the same applies to the simulated PA probe (i.e., with notation of LM-5MHz, see Section 3.1). Within the scope and availability of *simSUNDT*, penny-shaped circular crack is chosen to represent the actual lack-of-fusion defect in simulations [57]. The identified inspection parameters for this inspection scenario, including PA probe parameters, defect and material characteristics, can be characterized into two groups, namely essential parameters and influential parameters. The essential parameters are the ones having large impact on the results, while the influential parameters have little impact and can thus be set as constant at their nominal values in simulations. To imitate the probabilistic behavior of inspection process experienced in experiments, it is necessary to introduce minor variations to essential parameters using uncertainty propagation method [58]. This method specifies individual uncertainty ranges and distributions (parameter space) to each essential parameter so that the uncertainties and variations encountered in experiments are represented. With the help of sensitivity analysis, it is possible to identify essential parameters as well as influential parameters for this inspection scenario, see Table 4.1. Besides, all material-related properties (wave velocities) are set as constant. The focusing depth of the PA probe is also set as constant even though it has large impact and this is accomplished by proper calibration before the inspection. Note that the defect size are called characteristic parameter and is chosen in this work as diameter of the circular crack, against which the POD curve is plotted. Simulations

Table 4.1: Essential and influential parameters (parameter space) in the considered inspection scenario

Group	Parameter	Distribution	Mean	Standard deviation	Delta	Range´
Characteristic	Defect size	Uniform				[0.5: 5] mm
Essential	Defect depth	Uniform	25 mm	2.67	5 mm	[20: 30] mm
	Defect tilt angle	Normal	0°			[-10: 10]°
	Defect skew angle	Uniform	0°		90°	[-90: 90]°
Influential	Beam angle		0°			
	Probe skew angle		0°			
	Focusing depth		25 mm			

are then performed in this parameter space to generate a spread of inspection results (the maximum echo amplitude is taken as the resulted signal response). The decision threshold ($\hat{a}_{dec}$ in Equation (4.5)) is chosen to be 6 dB drop from a calibration defect, which is a SDH with 0.5 mm in diameter and 25 mm in depth in the same inspection scenario as all defects.

To better represent the physical situation compensating for material attenuation and sound beam spread and to explore the POD results further, a modified *Distance Amplitude Correction/Time Varied Gain (DAC/TVG)* function is applied in post-processing the calibrated inspection data. The reference reflectors are FBHs of the same size at different depth between 20 and 30 mm, covering the whole test volume of inspections, i.e., the depth where actual defects locate (see Table 4.1). Inspections on these reference reflectors are simulated in the same configuration as actual defects, and the corresponding time-varied gains are calculated relative to the maximum echo amplitude of reference reflector (standard level, A_s), see Figure 4.4. The two blocks in the figure use different FBH sizes, i.e., Block 1 has FBH size of 0.5 mm and Block 2 has size 5 mm. Note that the valley shape of these modified-TVG curves come from the focused sound beam at 25 mm depth, where the echo amplitudes from FBHs reach maximum. The ultimate applied gains on defect echo amplitudes depend on the actual defect depths by interpolation.

4.2.6 Results

In total, 600 simulations are performed for the inspection scenario in the parameter space (Table 4.1) and calibrated. Corresponding TVGs from two blocks are also applied on the calibrated results. $POD(a)$ functions for these three cases are calculated as in Equation (4.7)-(4.9) and plotted in Figure 4.5.
Case 1: Calibrated echo amplitude without TVG compensation:

$$POD(a) = \Phi(-2.428 + 2.95 \ln(a)) \tag{4.7}$$

Case 2: Calibrated and TVG-compensated (Block 1):

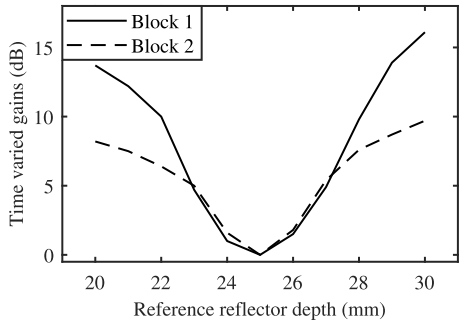

Figure 4.4: *Modified-TVG curves for two proposed reference blocks*

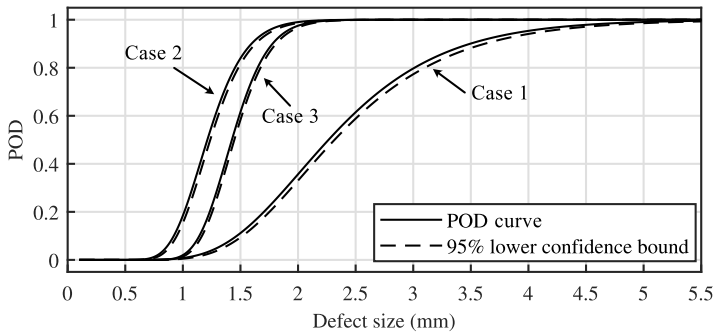

Figure 4.5: *POD curves and confidence bound for all three cases*

$$POD(a) = \Phi(-0.916 + 4.67 \ln(a)) \tag{4.8}$$

Case 3: Calibrated and TVG-compensated (Block 2):

$$POD(a) = \Phi(-2.096 + 5.78 \ln(a)) \tag{4.9}$$

Defect size of 90% POD with 95% confidence, $a_{90/95}$, is 3.6 mm, 1.6 mm and 1.8 mm for the three respective cases. It is clearly shown that the resulted POD is improved with the modified-DAC/TVG in use, because the defect echo amplitudes are systematically compensated with certain gains depending on their depth.

Before the actual $POD(a)$ function is calculated, there were some observed violations of log-normal POD model assumptions in calibrated echo amplitudes from defects, i.e., non-normal distribution of $\ln(\hat{a})$ and varied standard deviation dependent on defect sizes in Equation (4.4). This has to be verified somehow.

Taking the advantage of numerical simulation, it is possible to create a meta-model of inspected signal response. In other words, a Response Surface Model

(RSM). It is an approximate mathematical representation of complex model responses, trained based on a series of time-consuming simulation results from original mathematical model. The created metamodel can then provide fast estimations of the model response. To get statistically sufficient number of inspection results, the metamodel is used to estimate 5000 inspection data for a defect size. Then a discrete POD value of this defect size is estimated using Equation (4.1) and the same detection criteria (6 dB drop from calibration) as previous. The resulted discrete POD values are plotted in Figure 4.6 for above three cases.

It can be briefly concluded from Figure 4.6 that the POD curves based on log-normal POD model show good correlations in trend to the discrete POD values. The curves underestimate the POD for defect sizes larger than about 1.3 mm for all cases. When it comes to the previous mentioned violations of model assumptions, it is noticed from all these 5000 simulations that not all discrete POD values converge to 1 above some certain sizes of defect. This indicates that there are still a portion of cases giving resulted echo amplitudes below the decision threshold of -6 dB, and that part of these cases could still present violations of model assumptions including normal distribution and uniform standard deviation. However, the comparisons in Figure 4.6 show no necessity of this concern.

4.3 Investigation of TFM by simulated FMC dataset

With the increasing application of ultrasonic arrays techniques in industries and the knowledge that FMC dataset contains a full set of inspection information, it is beneficial to expand the capability of *simSUNDT* to generate simulation-based FMC dataset given a specific inspection scenario. This could provide a base for some parameter studies of e.g., the TFM algorithm.

4.3.1 Generating FMC dataset by simSUNDT implementation

Given the UT modelling principle as introduced in Section 2.4 and the available tandem probe configuration in *simSUNDT*, it is possible to emulate FMC data acquisition scheme and obtain A-scan signals from all available transmitter-receiver pairs of a PA probe by specifying the position of transmitting and receiving elements. This process at this stage is practically implemented through launching *simSUNDT* kernel (*UTDefect*) via Matlab script with certain input parameters of an inspection scenario. For a linear PA probe used in validation work, i.e., LM-5MHz with 64 elements (Figure 3.1(right)), 4096 A-scans in total can be generated and stored as a FMC dataset. This probe is also simulated in all relevant studies with its parameters introduced in Section 3.1.

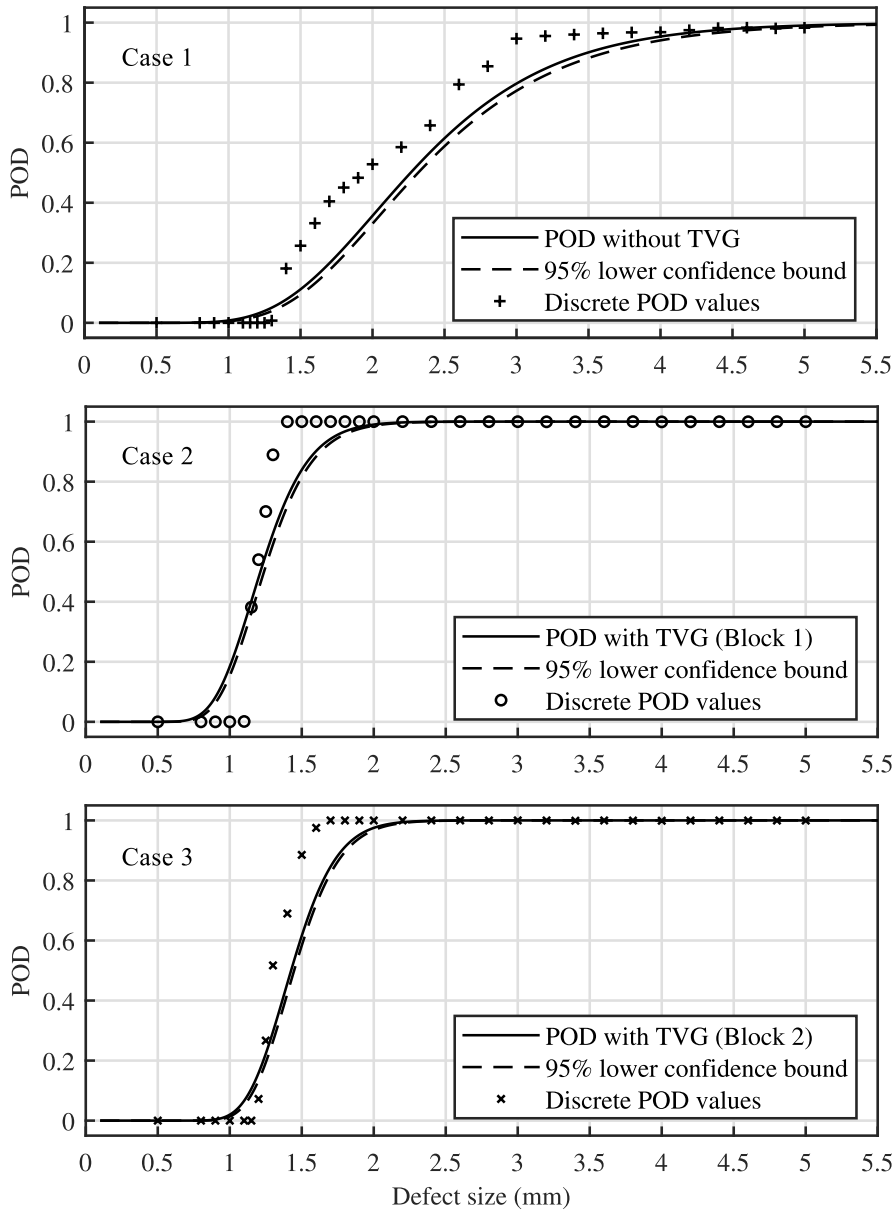

Figure 4.6: *Comparison between POD curve and corresponding discrete POD value points at some defect sizes for all three cases*

4.3.2 Snell's law based wave mode conversion in half-skip TFM

As introduced in Section 2.3 that the TFM algorithm can be grouped by three modes (direct, half-skip and full-skip) depending on the presumed imaging reconstruction path. In terms of half-skip TFM (HSTFM), one of the wave path, either transmitting or receiving, includes a reflection at the specimen backwall before or after reaching the imaging pixel. It is on the backwall that the wave mode conversion could happen and is considered here.

In conventional HSTFM, a general wave path of backwall reflection is found simply by connecting a line from the transmitting element (tr) to a mirror pixel (P_m) of the image pixel (P) over the backwall, see the dashed line in Figure 4.7(a). The intersecting point between this dashed line and backwall is the point of bounce. The wave path that reflects over the backwall is then equivalent to the mirrored path within the specimen. In this way, mode conversion in conventional HSTFM could be addressed by assigning corresponding wave speed at individual wave path (dashed line of L_1 and L_2 in Figure 4.7(a)) to calculate total TOF of wave [59]. However, this process could be inaccurate as the wave path and its length is different if Snell's law is to be satisfied at reflection, see the solid line in Figure 4.7(a). The local illustration of this in Figure 4.7(b) shows that the reflected wave angle θ_r should be different to incident angle θ_i according to Snell's law in Equation (2.2). Thus, the actual point of bounce, B, is different to the one in conventional HSTFM. In other words, to involve the Snell's law into wave mode conversion in HSTFM is hereby to find the actual position of point B in calculation of each wave path and length to the imaging pixel. This can be accomplished through rewriting Snell's law in form of Equation (4.10) as a function of the position of point B, and express the angles by corresponding coordinates, see more details in **Paper D** and **Paper E**. The position of point B can then be found by setting Equation (4.10) equals to zero so that Snell's law is in this way satisfied.

$$f = \frac{\sin\theta_i}{v_i} - \frac{\sin\theta_r}{v_r} \tag{4.10}$$

4.3.3 Parametric studies of defect characterization using HSTFM

With the possibility of simulating FMC dataset using *simSUNDT*, parametric studies are made feasible to explore the defect characterization capabilities using HSTFM images with varying defect features. Note that the Snell's law based wave mode conversion in Section 4.3.2 is always included in HSTFM algorithm in upcoming studies. The general inspection scenario studied here is shown in Figure 4.8, which is based on the surface-breaking EDM notch of size (d) 5 mm in

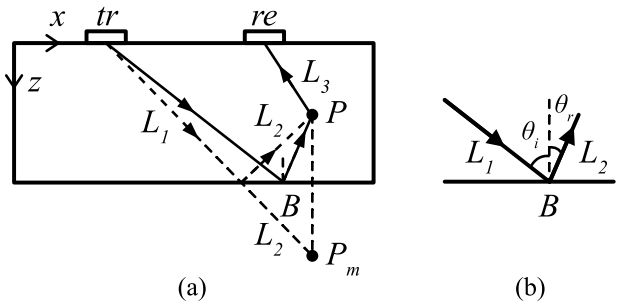

Figure 4.7: *(a) Reflection part of wave path (L_1 and L_2) in conventional HSTFM algorithm (without involving Snell's law, dashed line) and in proposed method (with Snell's law involved, solid line). (b) Local illustration of wave reflection at specimen backwall*

test specimen #2 (refer to Table 3.1 for acoustic properties and Figure 3.5(b) for appearance), which has height $h = 35$ mm. The ultrasonic PA probe LM-5MHz (effective length in x-direction $l = 38.3$ mm) is simulated to be placed on top surface of the specimen and the origin of coordinate system is placed at bottom-left of the array probe. The relative position between probe center and notch root is defined by an angle, θ_{test}, and positive tilt angle of the notch θ_{tilt} is defined in clockwise direction in parametric studies and simulations.

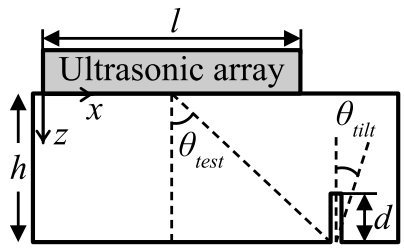

Figure 4.8: *Schematic illustration of the inspection scenario for parametric studies*

In the parametric studies, the notch tilt angle (θ_{tilt}) and the relative position of notch root to probe center (θ_{test}) are to be varied and investigated.

The first set of studies are under the condition of $\theta_{test} \approx 36°$. This is to ensure that the lateral distance between the center of probe and notch root is larger than half of the probe length in x-direction, i.e., $h * \tan\theta_{test} > l/2$, so that the potential indication of notch in HSTFM images are not covered and interfered by image artifacts induced by backwall reflection signals in certain wave mode sequences of HSTFM [60]. FMC datasets are collected with θ_{tilt} equals 0° and

between 15° and 45° at interval of 5°.

The second set of studies are under the condition of $\theta_{test} \approx 0°$. In this case, simulations by *simSUNDT* have an advantage over experiments that the unnecessary backwall reflection signals can be excluded [61], so that the corresponding image artifacts could be eliminated. This study could provide an insight of defect characterization using HSTFM images if the backwall reflection signals could be perfectly removed from experimental FMC datasets. FMC datasets are simulated with θ_{tilt} equals 0°, 20° and 45°.

4.3.4 Results

For the verification of Snell's law based HSTFM (**Paper D**), the experimental FMC dataset is collected according to the setup in Figure 4.8, where $\theta_{test} \approx 36°$ and $\theta_{tilt} = 0°$, see Figure 4.9. Simulated FMC dataset is also collected as in Section 4.3.1 as a complement and verification.

Figure 4.9: *Experimental inspection setup to collect FMC dataset*

Due to the sensitivity of TFM image modes to defect features, only certain TFM images are useful in defect characterization [33]. It is observed in HSTFM images of wave mode sequence LTT (L stands for longitudinal wave and T for transverse wave, in sequence of L_1, L_2 and L_3 in Figure 4.7(a)) from both experimental and simulated FMC dataset that the upright notch in Figure 4.9 can be correctly indicated when Snell's law based wave mode conversion is included in HSTFM algorithm, see Figure 4.10(a) and (c), while the exclusion of it would influence the notch indication in terms of tilt angle, see Figure 4.10(b) and (d), which could mislead defect interpretations and characterizations.

When it comes to the parametric studies of defect characterization capability using HSTFM (**Paper E**), all wave mode sequences of HSTFM images are reconstructed for every FMC dataset. For the first set of studies where $\theta_{test} \approx 36°$ and θ_{tilt} equals 0° and between 15° and 45° at interval of 5°, only the mode LLT, LTT, TTT and TLT could give a clear indication of the notch. It is also possible to identify the tilt angle of the notch by connecting the center of notch

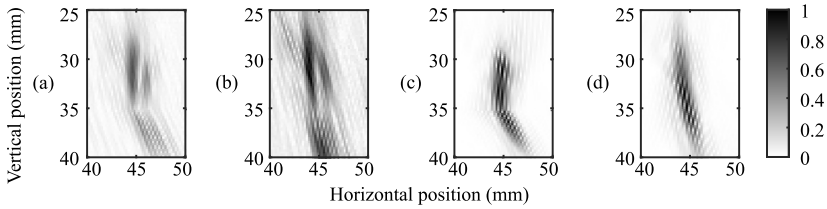

Figure 4.10: *Reconstructed HSTFM images in LTT wave mode sequence based on experimental FMC dataset (a) with Snell's law based wave mode conversion and (b) without Snell's law based wave mode conversion. They are complemented with images of the same wave mode sequence using simulated FMC dataset (c) with Snell's law based wave mode conversion and (d) without Snell's law based wave mode conversion*

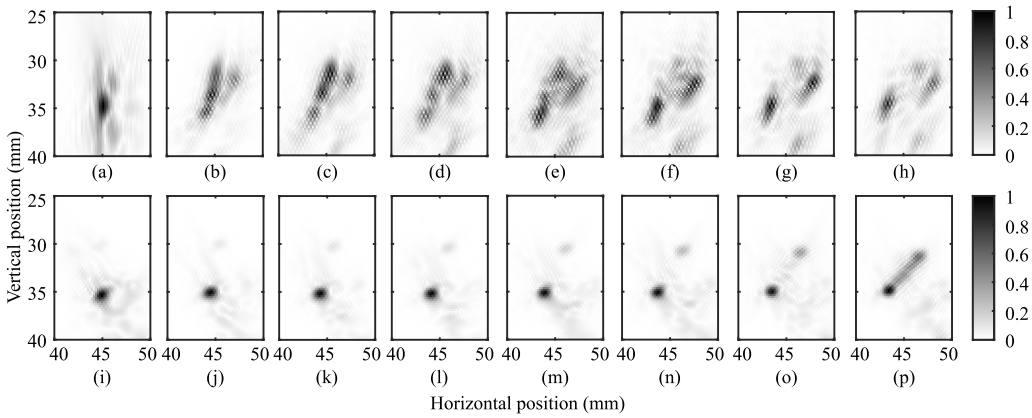

Figure 4.11: *(a) Reconstructed HSTFM images in LLL wave mode sequence based on simulated FMC dataset with $\theta_{tilt} = 0^{\circ}$ and (b)-(h) in LLT wave mode sequence with $\theta_{tilt} = 15^{\circ}$, 20°, 25°, 30°, 35°, 40° and 45°. (i)-(p) Reconstructed direct path TFM images in LL wave mode sequence for corresponding θ_{tilt}.*

tip and root indications. Mode LLT seems to be able to indicate correct tilt angles until 25°, see Figure 4.11(b)-(h), while the results from other modes are always smaller than actual values. It is also noticed that the notch profile can be better visualized by direct path TFM (mode LL) when tilt angle approaches 45°, see Figure 4.11(i)-(p). For the second set of studies where $\theta_{test} \approx 0^{\circ}$ and θ_{tilt} equals 0°, 20° and 45°, none of the modes can indicate the non-zero tilt angles correctly and the notch indications are interfered with image artifacts induced by notch signals. It is concluded inappropriate to characterize the defect using this setup when the probe projection area covers the defect. More details and pictures can be read in **Paper E**.

5 Summary of appended papers

5.1 Paper A

The newly developed and implemented phased array probe model in *simSUNDT* for advanced ultrasonic testing is further validated by comparing the simulation results with corresponding experiments, in terms of the maximum echo amplitudes. To master the experimental process and data, a mechanized gantry system and platform was built at the NDT lab of the Scientific Center of NDT (SCeNDT) at Chalmers University of Technology, on which all experiments were performed. Two test specimens with Side-drilled Holes (SDHs), considered as predefined artificial defects and different materials are involved for validation and practical purposes. Good correlations can be seen from the comparisons and this model is concluded as an acceptable option to the corresponding experimental work. In addition, the relation between depth and the true beam angle is investigated, which is essential to guarantee an accurate inspection. This is also to show the flexibility of parametric studies using a simulation model.

5.2 Paper B

The model validation work further continues in this paper by various data presentation comparisons with corresponding experimental results, i.e. ultrasonic A-, B- and C-scans. The defect types considered are Side-drilled Holes (SDHs) and Electric Discharge Machined (EDM) notches, where the direct echo and corner echo are the respective received signals. The EDM notches are simulated by surface-breaking cracks based on the scope and availability of the model. The comparisons show generally satisfactory correlations in different data presentations. After this validation of the model, it is then applied in sound field optimization. The optimization addresses searching for a proper combination of main beam angle and focus distance at this stage, so that a maximized echo amplitude towards a certain defect, which has specific characters (size and tilt angle), can be retrieved. The initial methodology of the optimization process is investigated in this paper.

5.3 Paper C

The validated phased array probe model is applied in a simulation-based investigation of a Probability of Detection (POD) model (cumulative log-normal POD model, also referred as Probit model). This is motivated by the basic assumptions involved in this POD model, and that little information is available

regarding the verification of itself provided that the basic assumptions are not fully satisfied. An inspection scenario is studied for this purpose, where Phased Array Ultrasonic Testing (PAUT) is applied on lack-of-fusion defects in additive manufacturing components. The target defect type of lack-of-fusion is simulated as penny-shaped circular crack considering the scope and availability of simulation model in *simSUNDT*. The probability nature of Nondestructive Evaluation (NDE) is represented using uncertainty propagation method so that the simulations can generate a spread of inspection results as in physical experiments. A modified Distance Amplitude Correction / Time Varied Gains (DAC/TVG-mod) function is proposed with the intention of further exploring the inspection data in post-processing. To facilitate efficient and fast computations, a Response Surface Model (RSM), or in other words metamodel, is built based on a series of simulated results from *simSUNDT*. This metamodel helps generate a large amount of rapid estimations of inspection results, so that the log-normal POD model can be verified through comparing the resulted POD curves of different datasets with a series of discrete POD value points from the metamodel. The comparisons show good correlations even though there are a few inspection results violating the basic assumptions of the POD model when the DAC/TVG-mod function is used. It is in the end concluded that the log-normal POD model is still a satisfactory model to signal response type of inspection data and there is no need of concern about minor violation of POD model assumptions.

5.4 Paper D

The Total Focusing Method (TFM) is one of the imaging algorithms using Full Matrix Capture (FMC) ultrasonic testing data. It can be grouped into different modes by considering different sound wave paths in the test specimen. Half-skip TFM (HSTFM) as one of the modes, considers one of the sound wave path, either transmitting or receiving part, to be reflected at specimen backwall. This helps reconstruct the defect profile in TFM images so that the capability of defect characterization is improved and visualization is made possible. However, wave mode conversion could happen when the wave reflects at backwall, where the conventional HSTFM does not seem to take it into account properly. This might mislead the calculation of Time-of-Flight (TOF) of sound wave, which is key to the delay-and-sum process of TFM algorithm. This paper proposes a method that involves Snell's law into estimating the sound wave path, so that the TOF calculation in HSTFM is expected to be more accurate. The conventional and new HSTFM algorithm is applied to an experimental FMC dataset inspecting an upright Electric Discharge Machined (EDM) notch to verify the influence.

Clear discrepancies can be seen from the comparisons in certain wave mode sequence and it is concluded that the new algorithm is to be used to avoid possible misinterpretation in defect characterizations.

5.5 Paper E

To further develop the software *simSUNDT* and to explore its capabilities in field of ultrasonic array techniques, approaches have been taken to generate Full Matrix Capture (FMC) dataset through its mathematical kernel, *UTDefect*. This could provide a simulation base for parametric studies to investigate e.g., defect characterization capabilities using Total Focusing Method (TFM). A series of FMC datasets are simulated inspecting surface-breaking cracks with varying tilt angles and relative position to the array probe. All wave mode sequences of direct path and half-skip path TFM images are reconstructed on these FMC datasets to illustrate the ability of visualizing the defect profile. It is observed in some wave mode sequences that some of the defect tilt angles could be identified correctly and some wave mode sequences could be misleading with image artifacts. It is also concluded that different TFM modes should complement with each other when it comes to defect characterization.

6 Concluding remarks

With the increasing demands of quality and integrity of the manufactured components in industries utilizing advanced production technologies, ultrasonic inspection as one of the nondestructive evaluation methods plays an important role. To better understand the method and facilitate qualification procedures, corresponding numerical simulation models were developed, which are needed to go through experimental validations thoroughly.

In this thesis, a newly developed Phased Array (PA) Ultrasonic Testing (UT) probe model is validated by comparing simulation results with experiments, in terms of maximum echo amplitudes and different types of data presentations. This PA probe model was implemented into the ultrasonic testing simulation software, *simSUNDT*, developed at Scientific Center of NDT (SCeNDT) at Chalmers University of Technology. To stabilize all inspection operations and keep track of probe positions for data presentation, a mechanized inspection system is built at NDT lab at SCeNDT.

Good correlations are observed from these simulation-experiment comparisons in general (**Paper A and B**), and the PA probe model is hereby concluded as validated and can be treated as a complement to experiments. Notice is given to the limitations that the considered defect types at this stage are restricted to some well-defined artificial ones, e.g., side-drilled holes and surface-breaking defects. In addition, material damping and other sources of attenuation as well as probe contact conditions are not considered in all simulations in first place. This is because the focus was put on the validation of PA probe model itself.

The probe model is then used in several application attempts to investigate its applicability in for example, inspection technique developments and studies. This includes investigation of optimizing the sound field from a phased array probe (**Paper B**), verification of log-normal Probability of Detection (POD) model (**Paper C**) and parametric studies of the capability of defect characterization using half-skip Total Focusing Method (HSTFM) (**Paper D and E**).

For the sound field optimization, it intends to explore an optimized combination of main beam angle and focusing distance of the phased array probe towards a defect with certain features, so that the echo amplitude from this defect can be maximized. The probe model has shown possibilities of searching for optimal solution in this application and some unexpected results are found under this framework, which differ from the solution of instinct but have been experimentally verified.

In the simulation-based verification of POD model, it aims at providing a large amount of specific inspection data through simulations, and verifying the widely-

used statistical log-normal POD model by comparing its results with discrete value points under different situations. These situations are set so that the assumptions and conditions of the POD model can be explored and evaluated to some extent. It has been concluded from the observations that the log-normal POD model provides satisfactory results despite the model hypotheses could be violated in some inspection cases.

The investigation of the capability of defect characterization using HSTFM provide some insights of this technique along with the proposed new algorithm. This contributes to a more sensible and accurate handling of sound wave mode conversion at backwall reflection in HSTFM. The parametric simulations lay a precise base to this investigation and all possible HSTFM images, which present clear views on how HSTFM and what wave mode sequence helps in defect characterization.

There is space for further validations of this model. This could involve for example, more complex Additive Manufacturing (AM) related defect and material types. Besides, attenuation sources including material damping and probe-specimen contact conditions etc., could also be involved for more thorough discussions. The sound field optimization could be further proceeded on exploring optimized delay law of individual elements of the PA technique for better signal processing in the final stage. Regarding the software *simSUNDT*, the function of generating FMC dataset should preferably be implemented in future version.

References

[1] T. SELDIS. *ENIQ Recommended Practice 2 - Strategy and Recommended Contents for Technical Justifications (Issue 2). ENIQ report no 39*. EUR - Scientific and Technical Research Reports. Publications Office of the European Union, 2010.

[2] P. Calmon. Trends and stakes of NDT simulation. *Journal of Nondestructive evaluation* **31**.4 (2012), 339–341.

[3] F. Jensen et al. "Simulation based POD evaluation of NDI techniques". *10 th European conference on non-destructive testing, Moscow*. 2010.

[4] P. Calmon. Recent developments in NDT simulation. *WCU* (2003), 443–446.

[5] R. Raillon et al. "Results of the 2009 UT modeling benchmark obtained with CIVA: responses of notches, side-drilled holes and flat-bottom holes of various sizes". *AIP Conference Proceedings*. Vol. 1211. 1. American Institute of Physics. 2010, pp. 2157–2164.

[6] M. Garton et al. "UTSim: overview and application". *AIP Conference Proceedings*. Vol. 1211. 1. American Institute of Physics. 2010, pp. 2141–2148.

[7] R. Hill, SA. Forsyth, and P. Macey. Finite element modelling of ultrasound, with reference to transducers and AE waves. *Ultrasonics* **42**.1-9 (2004), 253–258.

[8] Z. Tang et al. FEM model-based investigation of ultrasonic TOFD for notch inspection. *Journal of the Korean Society for Nondestructive Testing* **34**.1 (2014), 1–9.

[9] P. Fellinger et al. Numerical modeling of elastic wave propagation and scattering with EFIT—elastodynamic finite integration technique. *Wave motion* **21**.1 (1995), 47–66.

[10] KJ. Langenberg and R. Marklein. Transient elastic waves applied to nondestructive testing of transversely isotropic lossless materials: a coordinate-free approach. *Wave Motion* **41**.3 (2005), 247–261.

[11] L. Azar, Y. Shi, and S-C. Wooh. Beam focusing behavior of linear phased arrays. *NDT & e International* **33**.3 (2000), 189–198.

[12] B. Puel et al. Optimization of ultrasonic arrays design and setting using a differential evolution. *NDT & E International* **44**.8 (2011), 797–803.

[13] S. Avramidis et al. "Ultrasonic modelling to design a phased array probe for the testing of railway solid axles from the end face". *52nd Annual Conference of the British Institute of Non-Destructive Testing 2013*. 2013, pp. 500–511.

[14] S. Chatillon et al. "Results of the 2014 UT modeling benchmark obtained with models implemented in CIVA: Solution of the FMC-TFM ultrasonic

benchmark problem using CIVA". *AIP Conference Proceedings*. Vol. 1650. 1. American Institute of Physics. 2015, pp. 1847–1855.

[15] G. Persson and H. Wirdelius. "Recent survey and application of the simSUNDT software". *AIP Conference Proceedings*. Vol. 1211. 1. American Institute of Physics. 2010, pp. 2125–2132.

[16] A. Boström and AS. Eriksson. Scattering by two penny-shaped cracks with spring boundary conditions. *Proceedings of the Royal Society of London. Series A: Mathematical and Physical Sciences* **443**.1917 (1993), 183–201.

[17] P. Bövik and A. Boström. A model of ultrasonic nondestructive testing for internal and subsurface cracks. *The Journal of the Acoustical Society of America* **102**.5 (1997), 2723–2733.

[18] H. Wirdelius. "Experimental validation of the UTDefect simulation software". *Proc. 6th Int. Conf. on NDE in Relation to Structural Integrity for Nuclear and Pressurized Components, Budapest*. 2007.

[19] World Federation of NDE Centers. *UT Benchmark studies*. URL: `https://www.wfndec.org/benchmark-problems/` (visited on 05/18/2020).

[20] H. Wirdelius. "The implementation and validation of a phased array probe model into the simSUNDT software". *Proceedings of 11th European Conference on NDT*. 2014.

[21] BW. Drinkwater and PD. Wilcox. Ultrasonic arrays for non-destructive evaluation: A review. *NDT & e International* **39**.7 (2006), 525–541.

[22] X. Lei. "Experimental Validation of a Phased Array Ultrasonic Testing Probe Model and Sound Field Optimization". Licentiate Thesis. Chalmers University of Technology, Gothenburg, Sweden, Oct. 2020.

[23] N. Kono and A. Baba. "Development of phased array probes for austenitic weld inspections using multi-gaussian beam modeling". *AIP Conference Proceedings*. Vol. 975. 1. American Institute of Physics. 2008, pp. 747–753.

[24] P. Wells. Ultrasonic imaging of the human body. *Reports on progress in physics* **62**.5 (1999), 671.

[25] VP. Karthik, J. Joseph, and S. Mohanasankar. "Measurement of Left Ventricular Parameters using Ultrasound Transducer–a preliminary study". *2018 IEEE International Symposium on Medical Measurements and Applications (MeMeA)*. IEEE. 2018, pp. 1–6.

[26] B. Shan and J. Ou. "An ultrasonic phased array system for NDT of steel structures". *Fundamental Problems of Optoelectronics and Microelectronics II*. Vol. 5851. International Society for Optics and Photonics. 2005, pp. 273–277.

[27] A. Lopez et al. Phased Array Ultrasonic Inspection of Metal Additive Manufacturing Parts. *Journal of Nondestructive Evaluation* **38**.3 (2019), 62.

[28] Y. Qin et al. An Improved Phased Array Ultrasonic Testing Technique for Thick-Wall Polyethylene Pipe Used in Nuclear Power Plant. *Journal of Pressure Vessel Technology* **141**.4 (2019).

[29] XE. Gros, NB. Cameron, and M. King. Current applications and future trends in phased array technology. *Insight(UK)* **44**.11 (2002), 673–678.

[30] C. Holmes, BW. Drinkwater, and PD. Wilcox. Post-processing of the full matrix of ultrasonic transmit–receive array data for non-destructive evaluation. *NDT & E International* **38**.8 (2005), 701–711.

[31] LW. Schmerr Jr. *Fundamentals of ultrasonic phased arrays*. Vol. 215. Springer, 2014.

[32] J. Zhang et al. Defect detection using ultrasonic arrays: The multi-mode total focusing method. *NDT & e International* **43**.2 (2010), 123–133.

[33] K. Sy et al. "Development of methods for the analysis of multi-mode TFM images". *Journal of Physics: Conference Series*. Vol. 1017. 1. IOP Publishing. 2018, p. 012005.

[34] Y. Peng and T. Gang. "The Use of Multi-Mode TFM to Measure the Depth of Small Surface-Break Cracks in Welds". *2017 Far East NDT New Technology & Application Forum (FENDT)*. IEEE. 2017, pp. 106–110.

[35] A. Boström and H. Wirdelius. Ultrasonic probe modeling and nondestructive crack detection. *The Journal of the Acoustical Society of America* **97**.5 (1995), 2836–2848.

[36] H. Wirdelius. Probe model implementation in the null field approach to crack scattering. *Journal of nondestructive evaluation* **11**.1 (1992), 29–39.

[37] BA. Auld. General electromechanical reciprocity relations applied to the calculation of elastic wave scattering coefficients. *Wave motion* **1**.1 (1979), 3–10.

[38] A. Boström and P. Bövik. Ultrasonic scattering by a side-drilled hole. *International Journal of Solids and Structures* **40**.13 (2003), 3493–3505.

[39] Peter J. Shull. *Nondestructive evaluation: theory, techniques, and applications*. CRC press, 2002.

[40] F. Sun et al. Sound-field of discrete point sources simulation on deflecting and focusing of near-field of ultrasonic phased array. *Xitong Fangzhen Xuebao / Journal of System Simulation* **25** (May 2013), 1108–1112.

[41] I. Grešovnik. *Simplex algorithms for nonlinear constraint optimization problems*. Tech. rep. 2009.

[42] GA. Georgiou. POD curves, their derivation, applications and limitations. *Insight-Non-Destructive Testing and Condition Monitoring* **49**.7 (2007), 409–414.

[43] AGARD Lecture Series. "A Recommended Methodology for Quantifying NDE / NDI Based on Aircraft Engine Experience". 1993.

[44] DS. Forsyth and A. Fahr. An evaluation of probability of detection statistics. *Institute of Aerospace Research* (1998), 10–1.

[45] AP. Berens and PW. Hovey. Evaluation of NDE reliability characterization. *Report No. AFWAL-TR-81-4160* (1981).

[46] BG. Yee et al. *Assessment of NDE Reliability Data.* Tech. rep. GENERAL DYNAMICS FORT WORTH TX FORT WORTH DIV, 1976.

[47] WD. Rummel. Recommended practice for a demonstration of non-destructive evaluation (NDE) reliability on aircraft production parts. *Materials Evaluation* **40**.9 (1982), 922–932.

[48] WH. Lewis et al. Reliability of nondestructive inspections-final report. *SAALC/MME* (1978), 76–6.

[49] AP. Berens. NDE reliability data analysis. *ASM Handbook.* **17** (1989), 689–701.

[50] SF. Burch, BA. Stow, and M. Wall. Computer modelling for the prediction of the probability of detection of ultrasonic corrosion mapping. *Insight-Non-Destructive Testing and Condition Monitoring* **47**.12 (2005), 761–764.

[51] RB. Thompson. "A unified approach to the model-assisted determination of probability of detection". *AIP Conference Proceedings*. Vol. 975. 1. American Institute of Physics. 2008, pp. 1685–1692.

[52] F. Schubert et al. "Simulation-Supported POD for Ultrasonic Testing–Recommendations from the PICASSO Project". *5th European-American Workshop on Reliability of NDE*. 2013.

[53] B. Yilmaz, D. Smagulova, and E. Jasiuniene. Model-assisted reliability assessment for adhesive bonding quality evaluation with ultrasonic NDT. *NDT E International* **126** (2022), 102596. ISSN: 0963-8695. DOI: https://doi.org/10.1016/j.ndteint.2021.102596. URL: https://www.sciencedirect.com/science/article/pii/S096386952100195X.

[54] H. Wirdelius and G. Persson. Simulation based validation of the detection capacity of an ultrasonic inspection procedure. *International Journal of Fatigue* **41** (2012), 23–29.

[55] M. Wall, FA. Wedgwood, and S. Burch. "Modelling of NDT reliability (POD) and applying corrections for human factors". *Proceedings of the 7th European Conference on NDT, Copenhagen, Denmark*. 1998.

[56] M. Wall and S. Burch. "Worth of modelling for assessing the intrinsic capability of NDT". *15th World Conference on Nondestructive Testing*. 2000, pp. 15–21.

[57] A. Boström and G. Wickham. On the boundary conditions for ultrasonic transmission by partially closed cracks. *Journal of Nondestructive Evaluation* **10**.4 (1991), 139–149.

[58] F. Jenson, E. Iakovleva, and N. Dominguez. “Simulation supported POD: methodology and HFET validation case”. *AIP Conference Proceedings*. Vol. 1335. 1. American Institute of Physics. 2011, pp. 1573–1580.

[59] E. Iakovleva et al. “Multi-mode TFM imaging with artifacts filtering using CIVA UT forwards models”. *AIP conference proceedings*. Vol. 1581. 1. American Institute of Physics. 2014, pp. 72–79.

[60] MV. Felice, A. Velichko, and PD. Wilcox. Accurate depth measurement of small surface-breaking cracks using an ultrasonic array post-processing technique. *Ndt & E International* **68** (2014), 105–112.

[61] A. Bostroem. *User guide to UTDefect Version 4: A Computer Program Modelling Ultrasonic Nondestructive Testing of a Defect in an Isotropic or Anisotropic Component*. Tech. rep. Swedish Nuclear Power Inspectorate, 2002.